(This is a sample cover image for this issue. The actual cover is not yet available at this time.)

International Journal of Heat and Mass Transfer 57 (2013) 786–811

Contents lists available at SciVerse ScienceDirect

International Journal of Heat and Mass Transfer

journal homepage: www.elsevier.com/locate/ijhmt

Simulation of flow and heat transfer in a liquid drop sliding underneath a hydrophobic surface

Basant Singh Sikarwar, Sameer Khandekar *, K. Muralidhar

Department of Mechanical Engineering, Indian Institute of Technology Kanpur, Kanpur 208016, India

ARTICLE INFO

Article history:
Received 17 September 2011
Accepted 19 February 2012

Keywords:
Sliding liquid drop
Textured surface
Apparent contact angle
Shear stress
Heat transfer
Finite volume method

ABSTRACT

Clusters of liquid drops growing and moving on physically or chemically textured surfaces are encountered in dropwise mode of vapor condensation. This process can be sustained only if the surface integrity is maintained over a long period of time. Surface features are altered when sliding drops leach away the promoter layer. In the absence of chemical reactions between the promoter and the condensing liquid, the wall shear stress is the primary parameter controlling the physical leaching. In turn, wall shear stress depends on the relative speed between the drop and the substrate surface and the shape of the drop. Given a wall shear stress distribution for individual drops, the net effect of an ensemble of them during continuous quasi-steady state dropwise condensation can be determined using the population density of drops.

Wall shear stress and local heat fluxes have been determined in the present work by solving the Navier–Stokes and energy equations in three-dimensions on an unstructured tetrahedral grid that represents an individual droplet. The drop size and relative velocity are parameterized by the Reynolds number (Re = 10–1000), apparent contact angle (90–120°) and its shape. The simulations presented here are for a wide range of Prandtl numbers, i.e., 0.005–30. The wall shear stress and wall heat flux are expressed in terms of the skin friction coefficient and the Nusselt number, respectively. While these two quantities show an increase with Reynolds number, they decrease at higher values of the drop contact angle on/underneath hydrophobic surface. At low Prandtl numbers, heat transfer is mainly diffusional and the wall Nusselt number is practically independent of Reynolds number at any given Pr. The maximum wall shear stress as well as heat flux occurs at the corners of the drop close of the three-phase contact line. The surface averaged shear stress and heat flux are expressed in terms of appropriate correlations that include Reynolds number, Prandtl number, and the apparent contact angle. The wall shear stress in the relatively inactive central region at the drop base is smaller than the overall base average by a factor of 6, while that for heat transfer, the corresponding factor is in the range of 1.3–1.8. The figure of merit function, represented by the ratio of average Nusselt number to the friction coefficient, increases with contact angle, indicating an advantage to be gained from hydrophobic surfaces. The information presented in this paper is vital for further improvement of the available models of dropwise condensation on textured surfaces.

1. Introduction

The sliding of liquid drops over and underneath textured surfaces has been a subject of extensive research in the context of many engineering applications. These include examples such as dropwise condensation, microfluidics, lab-on-chip devices, ink jet printing systems, spraying of insecticide on crops and several biochemical processes [1–3]. It is known that dynamic steady-state of condensing vapor on a cold substrate involves a large population of drops of varying sizes, involving various generations [4,5]. The drops increase in size by a combination of direct condensation and/or coalescence with neighboring drops [6]. As drops grow, the body forces eventually exceed the drop retention force due to surface tension, leading to sliding of drops and fall off thereafter [7]. This step exposes virgin substrate for condensation, where a new generation of drops begins to grow [6,8]. The effective heat transfer coefficient during dropwise condensation is considerably greater than that for a liquid film condensation mode, making the former ideal from a heat transfer enhancement and energy conservation perspective [9].

The long term sustainability of dropwise condensation on a given substrate depends on the shear interaction of sliding drops with the hydrophobicity promoter layer [10]. The phenomenon of removal of this promoter layers, or surface damage due to sliding of drop, leads to surface leaching. It arises primarily from

* Corresponding author. Tel.: +91 512 259 7038; fax: +91 512 259 7408.
E-mail address: samkhan@iitk.ac.in (S. Khandekar).

0017-9310/$ - see front matter © 2012 Elsevier Ltd. All rights reserved.
http://dx.doi.org/10.1016/j.ijheatmasstransfer.2012.10.066

Nomenclature

C	Cell center of tetrahedron
C_p	specific heat of liquid (J/kg K)
d	base diameter of the drop measured on the solid substrate (m)
f	face center of tetrahedron
g	gravitational acceleration (m/s^2)
H	height of cavity (m)
h	local heat transfer coefficient (W/m^2 K)
$\overline{h}$	average heat transfer coefficient (W/m^2 K)
$\hat{i}$,$\hat{j}$ and $\hat{k}$	unit vectors in x, y and z directions
k	thermal conductivity (W/m K)
n	unit normal vector drawn on the drop surface (–)
P	vertices of the grid cell (–)
p	pressure (Pa)
q	heat flux (W/m^2)
t	time (s)
t_1 and t_2	unit tangent vectors over the surface of the drop (–)
T	temperature (°C)
ΔT	temperature difference between the substrate and the drop boundary (°C)
u	velocity component in x direction (m/s)
v	velocity component in y direction (m/s)
w	velocity component in z direction (m/s)
U	sliding velocity of substrate (m/s)
V	volume of drop (m^3)
α	thermal diffusivity (m^2/s)
β	volumetric expansion coefficient (K^{-1})
μ	dynamic viscosity of liquid (Pa s)
θ	apparent contact angle (° or radians)
ρ	fluid density (kg/m^3)
τ	shear stress (N/m^2)
ϕ	general flow variable (–)

Non-dimensional parameters

C_f	local Skin friction coefficient, $\tau_{wall}/(2\rho U^2)$
$\overline{C_f}$	average Skin friction coefficient, $\overline{\tau_{wall}}/(2\rho U^2)$
Nu	local Nusselt Number, hd/k
$\overline{\mathrm{Nu}}$	average Nusselt number, $\bar{h}d/k$
Pr	Prandtl number, $\mu C_p/k$
Re	Reynolds number, $\rho U d/\mu$
Ra	Rayleigh number, $g\beta\,(T_h - T_c)H^3/\nu\alpha$

Dimensionless quantities

u/U	dimensionless velocity in x direction
v/U	dimensionless velocity in y direction
w/U	dimensionless velocity in z direction
$p/(\frac{1}{2}\rho U^2)$	dimensionless pressure
$(T - T_w)/\Delta T$	dimensionless temperature

Subscripts

adv	advancing angle
b	base of the drop
C	cell center of tetrahedron
Cb	cell center of boundary tetrahedron
f	face center of tetrahedron
fb	face center of boundary face
f_{123}	face of cell which have node P_1, P_2 and P_3
free	free surface of the drop
h, c	hot and cold surfaces
i	free indices
j	repeated indices
rcd	receding angle
x, *y*, *z*	component in the x, y, or z direction, respectively
xy	x–y plane
yz	y–z plane
n	component in the normal direction, curvilinear coordinates
t_1, t_2	component in the tangential direction, curvilinear coordinates
wall	condensing wall surface

viscous forces at the contact surface and chemical reactions between the condensing liquid and the promoter. Heat transfer rates and temperature fluctuations affect these interactions [11]. A detailed analysis of viscous forces that lead to substrate leaching is sparse and forms the motivation of the present work.

Literature on surface leaching due to drop motion is limited. Most of the existing work [12–17] have considered the critical state of a static sessile drop on an inclined surface and focused on the apparent contact angle hysteresis, drop shape, and drop retention with tiltable surfaces, for various combinations of the hydrophobic substrates and liquids. Elsherbine and Jacobi [16–17] performed experiments on an isolated sessile drop and reported that the drop is deformed at the critical state over an inclined substrate. The geometric parameters necessary to describe the shape of the deformed drop at the critical state over an inclined substrate, and corresponding retention forces, were investigated. Though a large volume of work exists on predicting the drop shape under static conditions, only a few researchers have reported the sliding behavior of the drop on an inclined surface [18–28]. Kim et al. [18] performed experiments for measuring the steady sliding velocity of liquid drops on an inclined surface and reported a scaling law to determine the sliding velocity of a liquid drop of known wetting characteristics. Huang et al. [19] used a front tracking method to determine the motion of two-dimensional drops and bubbles on a partially wetting surface exposed to shear flow. Gao and McCarthy [20] postulated two mechanisms for drop moving down an inclined plane. Drops can move by sliding, where the particles near the solid-liquid interface exchange their position with those at the gas-liquid interface while the bulk of the fluid remains unaffected. The particle movement along the gas- liquid and solid-liquid interfaces is compared to the motion of a tread of a chain-driven tank. On the other hand, there could be rolling motion, where the entire fluid mass undergoes a circulatory movement. Suzuki et al. [21] studied the sliding behavior of water drops on various chemically textured surfaces at a fixed inclination of 35° and reported sliding displacement of the advancing edge of the drop. Sakai et al. [22] studied rolling versus sliding behavior of drops on various chemically textured surfaces. In their theoretical analysis, Grand et al. [23] scaled the viscous force as $\mu U V^{1/3}$ for a drop of volume V moving with a speed U and reported that the sliding velocity along an inclined plane is a linear function of the Bond number. Yoshida et al. [24] did not consider viscous forces in their study of sliding behavior of water drops on a flat polymer surface. The authors reported that the sliding motion changes from constant velocity to one of constant acceleration with an increase in the apparent contact angle. Daniel et al. [25] reported the maximum velocity of the condensing sessile drop on a chemically textured horizontal substrate having a wettability gradient. Sakai

and Hashimoto [26] have experimentally determined the velocity vector distribution inside a sliding sessile drop using PIV. The authors reported that the velocity gradient near the liquid-solid interface is higher than locations elsewhere inside the drop. This analysis was further used to recognize the slipping and rolling components of the sliding velocity and the acceleration of the water drop [27]. Das and Das [28] used smooth particle hydrodynamics to numerically simulate the movement of drops down an inclined plane. The study captured fluid circulation inside a sliding sessile drop. It was shown that the frictional resistance at the three-phase contact line cannot be neglected in estimating the sliding behavior and related effects, for a drop moving on an inclined substrate.

To the knowledge of the authors there is no literature available that correlates drop shape and speed with wall shear stress (skin friction coefficient) and heat transfer coefficient (Nusselt number) of an isolated drop sliding underneath a textured surface. The present work is aimed at providing a transport correlation for the friction factor and Nusselt number, as a function of Reynolds number, Prandtl number, and apparent contact angles. For this purpose, the three-dimensional Navier–Stokes and energy equations are solved by a finite volume method. An unstructured grid has been used for this purpose. The finite volume implementation closely follows the work of Date [29] for pressure correction.

The drop is taken as hemispherical for a horizontal surface and a variant of this shape is used for an inclined surface (see Fig. 1). Droplets move on an inclined surface whenever the net body forces exceed the retention force. This fluid movement leads to (a) apparent contact angle hysteresis, and, in addition, (b) additional changes in the interface shape due to velocity induced local pressure variation. In this work, only the former effect is included and therefore, the results reported here are to be taken as applicable for baseline configurations of the drop shapes.

The text below is arranged in the following manner. Section 2 of the paper describes the mathematical formulation of the problem and defines the non-dimensional numbers of interest. Section 3 is an outline of the numerical scheme with the details of implementation of the free surface boundary condition over the drop surface. Section 4 describes grid independence studies and code validation against well-known analytical and experimental data. Results and discussions are presented in Section 5 and finally, conclusions are reported in Section 6.

2. Mathematical formulation

The schematic diagram of a symmetric three-dimensional drop with various apparent contact angles (θ) and a deformed drop with an advancing angle (θ_{adv}) and a receding angle (θ_{rcd}) are shown in Fig. 1. During sliding motion, the flow field set up within the drop would alter the pressure distribution and hence the shape of drop free surface [14–15,30]. To a first approximation, this dynamic effect on the shape of the drop is neglected in the present study. The deformed drop with $\theta_{adv} = 105^\circ$ and $\theta_{rcd} = 55^\circ$ corresponds to a static drop placed over a substrate of nearly 30° inclination. All 3D shapes of the drops considered here (symmetric drops on horizontal substrate as well as deformed drops on inclined surface) have been generated by the two-circle approximation [16,31]. The cross-sectional shape thus obtained, on the frontal-plane at $z = 0$ (Fig. 2), satisfies the Young–Laplace equation fairly accurately for typical drop-sizes as encountered during dropwise condensation. This equation balances surface forces at the three-phase contact line while excess pressure and gravitational forces are included within. Symmetric drops are taken to be a part of sphere with a suitably chosen apparent contact angle (90°, 105° and 120°). The volume of the drops considered for analyses is kept constant and is constrained while generating the drop shape. In flow calculations, the incompressibility constraint merges body forces with pressure, and need not be explicitly accounted for. The coordinate system is fixed to the liquid drop, thereby making it stationary, while the substrate has a constant translational velocity. As the degree of subcooling never exceeds 3–5 °C, the liquid phase is treated as incompressible and additional effects due to buoyancy and Marangoni effects have been neglected.

The governing equations for flow and heat transfer within an incompressible liquid drop are given in Cartesian tensor notation as follows:

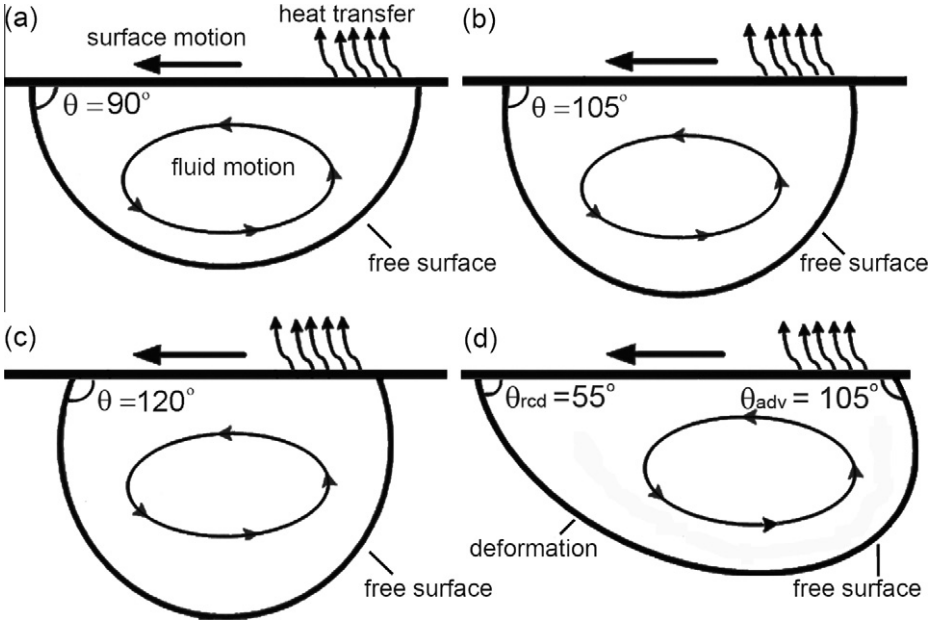

Fig. 1. Schematic diagram of flow inside a drop driven by wall motion. A symmetric drop with contact angles 90°, 105°, and 120° and a deformed drop ($\theta_{adv} = 105^\circ$ and $\theta_{rcd} = 55^\circ$) are shown. The volume of the drop is constant in (a)–(d). In non-dimensional form, wall velocity $U = -1$, while the wall and free surface temperatures are 0 and unity respectively.

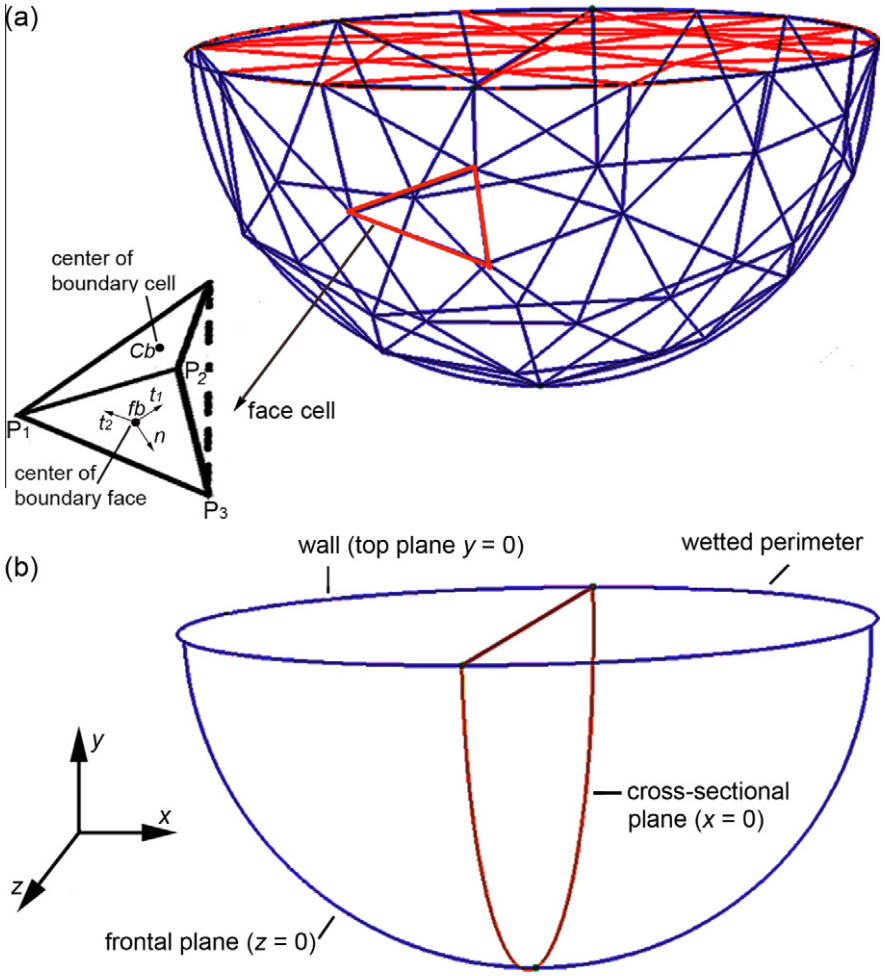

Fig. 2. Computational domain within a drop along with a tetrahedral grid and coordinate system. Triangular base of the tetrahedral element and large view of the boundary tetrahedron are shown in (a). (b) Representative planes of the drop for a contact angle of 90°.

$$\frac{\partial u_i}{\partial x_i} = 0 \tag{1}$$

$$\rho\left(\frac{\partial u_i}{\partial t} + u_j\frac{\partial u_i}{\partial x_j}\right) = -\frac{\partial p}{\partial x_i} + \mu\frac{\partial^2 u_i}{\partial x_j^2} \tag{2}$$

$$\rho C_p\left(\frac{\partial T}{\partial t} + u_j\frac{\partial T}{\partial x_j}\right) = k\frac{\partial^2 T}{\partial x_j^2} \tag{3}$$

These equations are written in Cartesian coordinates and solved for the Cartesian velocity components by the finite volume method. Boundary conditions are prescribed over the drop surface as follows. At the wall, the no-slip condition holds while the wall has a prescribed temperature. Hence,

$$u = U; \quad v = 0; \quad w = 0; \quad T = T_{wall} \tag{4}$$

The liquid boundary in contact with vapor is taken to be a stress-free surface. At the free surface, the pressure is constant, the normal component of velocity is zero and the shear stress components are also zero. The free surface is also taken to be isothermal at a given distinct temperature, the liquid–vapor thermal resistance being neglected. Hence,

$$u_n = 0; \quad \tau_{nt_1} = 0; \quad \tau_{nt_2} = 0; \quad T = T_{free} \tag{5}$$

The boundary conditions at the free surface are prescribed in curvilinear coordinates, n being the unit vector in the direction normal to the boundary face, while t_1 and t_2 are orthogonal tangential vectors at the boundary face, as shown in Fig. 2. They need to be transformed from the local curvilinear to Cartesian coordinates during numerical implementation. The details of implementation of the free surface boundary condition are described later.

Fluid flow and temperature distribution inside the drop are obtained by numerically solving the steady form of Navier–Stokes equations and energy equation in three dimensions with the appropriate boundary conditions (Eqs. (1)–(5)). In view of the small droplet sizes, the transients last only for very short durations and are therefore neglected. The flow and temperature fields are obtained for Reynolds numbers in the range 10–1000 for a range of Prandtl numbers covering liquid metals, water, and organic liquids (Pr ~ 0.005–30). Local wall shear stress and local wall heat flux are determined as follows:

$$\left.\begin{aligned}(\tau_{xy})_{wall} &= \mu\left[\tfrac{\partial u}{\partial y} + \tfrac{\partial v}{\partial x}\right]_{wall}\\ (\tau_{zy})_{wall} &= \mu\left[\tfrac{\partial w}{\partial y} + \tfrac{\partial v}{\partial z}\right]_{wall}\\ \tau_{wall} &= \sqrt{\tau_{xy}^2 + \tau_{zy}^2}\end{aligned}\right] \tag{6}$$

$$\left.\begin{aligned}q_{wall} &= -k\left[\tfrac{\partial T}{\partial n}\right] = -k\left[\tfrac{\partial T}{\partial y}\right]_{wall}\\ h &= \tfrac{q_{wall}}{\Delta T}\end{aligned}\right\} \tag{7}$$

The length scale chosen for the analysis is the base diameter of the drop while all parameters are evaluated at average temperature between the substrate and the drop interface. The definition of relevant non-dimensional numbers is given in the nomenclature.

3. Numerical solution

The numerical solution of the governing equations is developed as follows. The physical domain is subdivided into a number of contiguous control volumes on an unstructured grid. Three dimensional unstructured grids for the drop were generated using commercial software (ICMCFD). A typical computational domain with triangular faces on the boundary, tetrahedral elements inside the physical domain and the corresponding Cartesian coordinate system are shown in Fig. 2(a) for an apparent contact angle of 90°. Similar grids are generated for other symmetric and deformed drops. A tetrahedral cell which lies at the free surface is also shown with its local curvilinear coordinates (n, t_1 and t_2). The frontal-plane, the base of the drop and the cross-sectional plane, shown in Fig. 2(b), are chosen for presenting the simulation data.

Fig. 3 shows a tetrahedral control volume used for 3-D calculations. The finite-volume vertices are numbered as P_1, P_2, P_3 and P_4. The centroid of the main control volume is C, and the four neighboring control volume centers are indicated by C_1, C_2, C_3 and C_4, as shown in Fig. 3(a). The various faces of the tetrahedral volume cell and their face centers f_{123}, f_{234}, f_{341} and f_{412} are located at the corresponding face centroid of the control volume, Fig. 3(b). The numerical technique is based on the finite volume method (FVM), wherein the conservation laws are applied locally to control volumes. It lends itself to easy physical interpretation in terms of fluxes, source terms and the satisfaction of local conservation principles. In FVM, the governing equation is first integrated over a cell-volume and an integral form of the governing equation is obtained. The integral is replaced by summation and the required algebraic equation for the cell quantity is derived. In FVM derived on an unstructured grid, the mass balance and momentum Eqs. 1, 2 are to be decoupled first so that the velocity components and pressure are determined from explicit equations. Pressure-velocity decoupling is an extension of the SIMPLE algorithm and, except for a few differences in implementation, has been followed in the present study. In this approach, pressure (p) is determined via a pressure-correction equation that indirectly satisfies mass-conservation. On an unstructured mesh, it is most convenient to employ collocated variables so that scalar and vector variables are defined at the same location. For such a collocated arrangement, Date [29] has derived an equation for pressure correction with the aim of eliminating spatial fluctuations in the predicted pressure field. All geometric parameters for all control volumes were calculated in the preprocessing stage and stored for use during time stepping. Volume-weighted linear interpolation was used to find the face value, whenever required. Convective terms of the Navier–Stokes have been discretized using a higher-order upwind scheme, as discussed by Frink et al. [32].

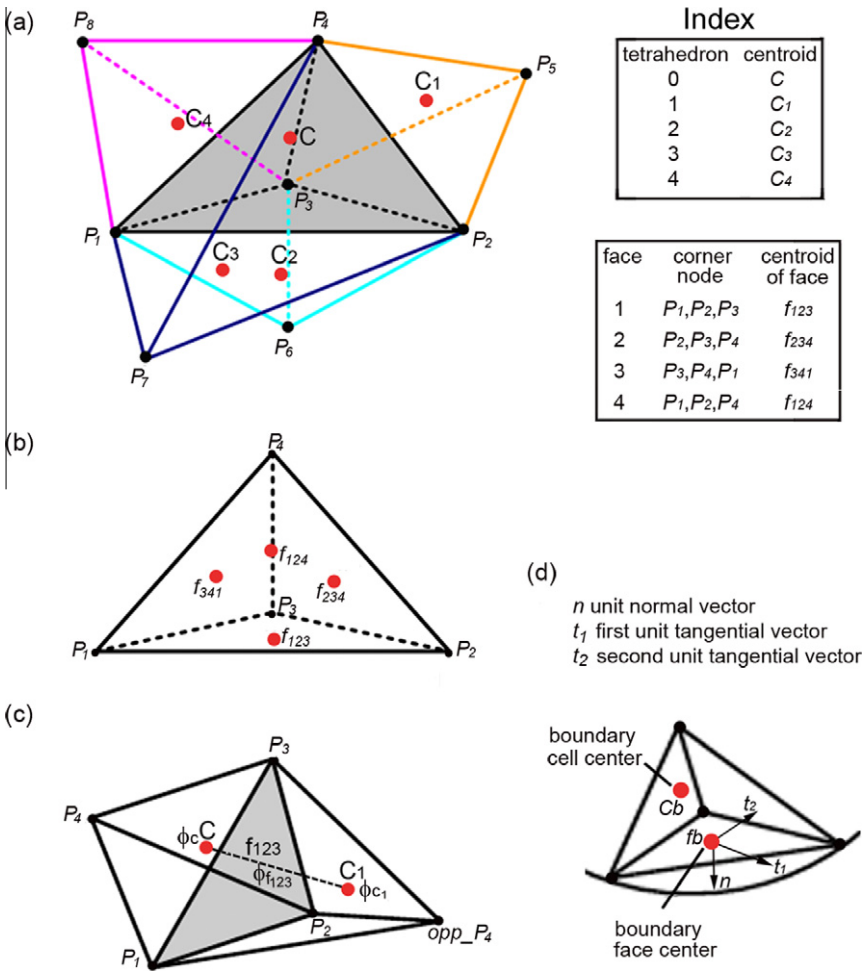

Fig. 3. (a) Three dimensional finite volume grid arrangement and collection of tetrahedra at an interior point with its four neighbors. (b) Tetrahedron as a finite volume element and its four faces. (c) Two tetrahedral with common face (f_{123}). (d) Boundary tetrahedron along with local curvilinear coordinates.

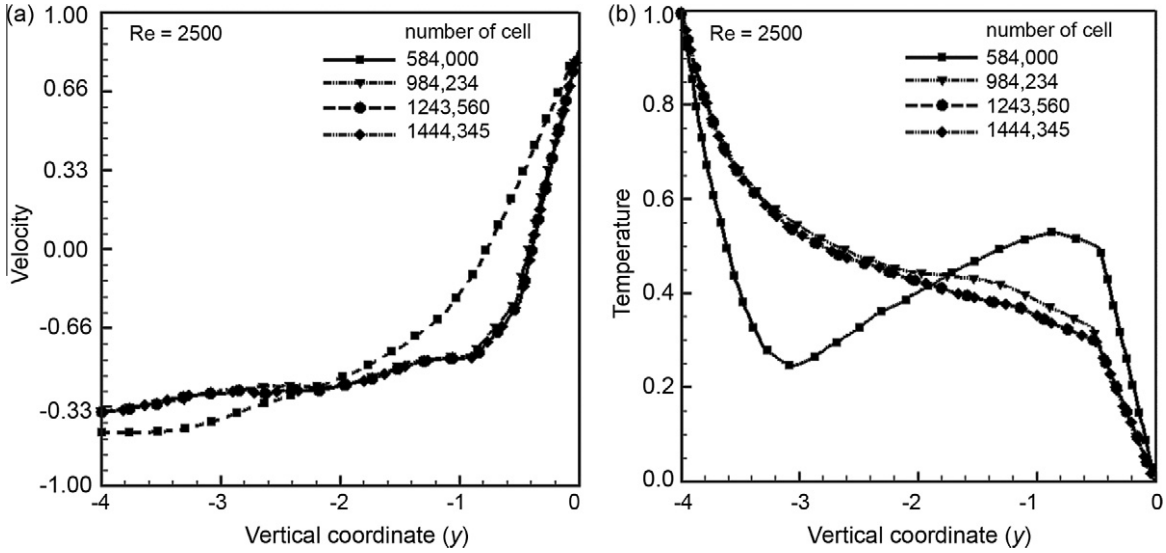

Fig. 4. Grid independence study for flow and heat transfer in a drop of contact angle 105° at various numbers of tetrahedral cells. (a) Profile of velocity component (u) with respect to the vertical coordinate (y); (b) Non-dimensional temperature profile with respect to the vertical coordinate (y), over the frontal plane (x–y,$z = 0$) of the drop. Re = 2500.

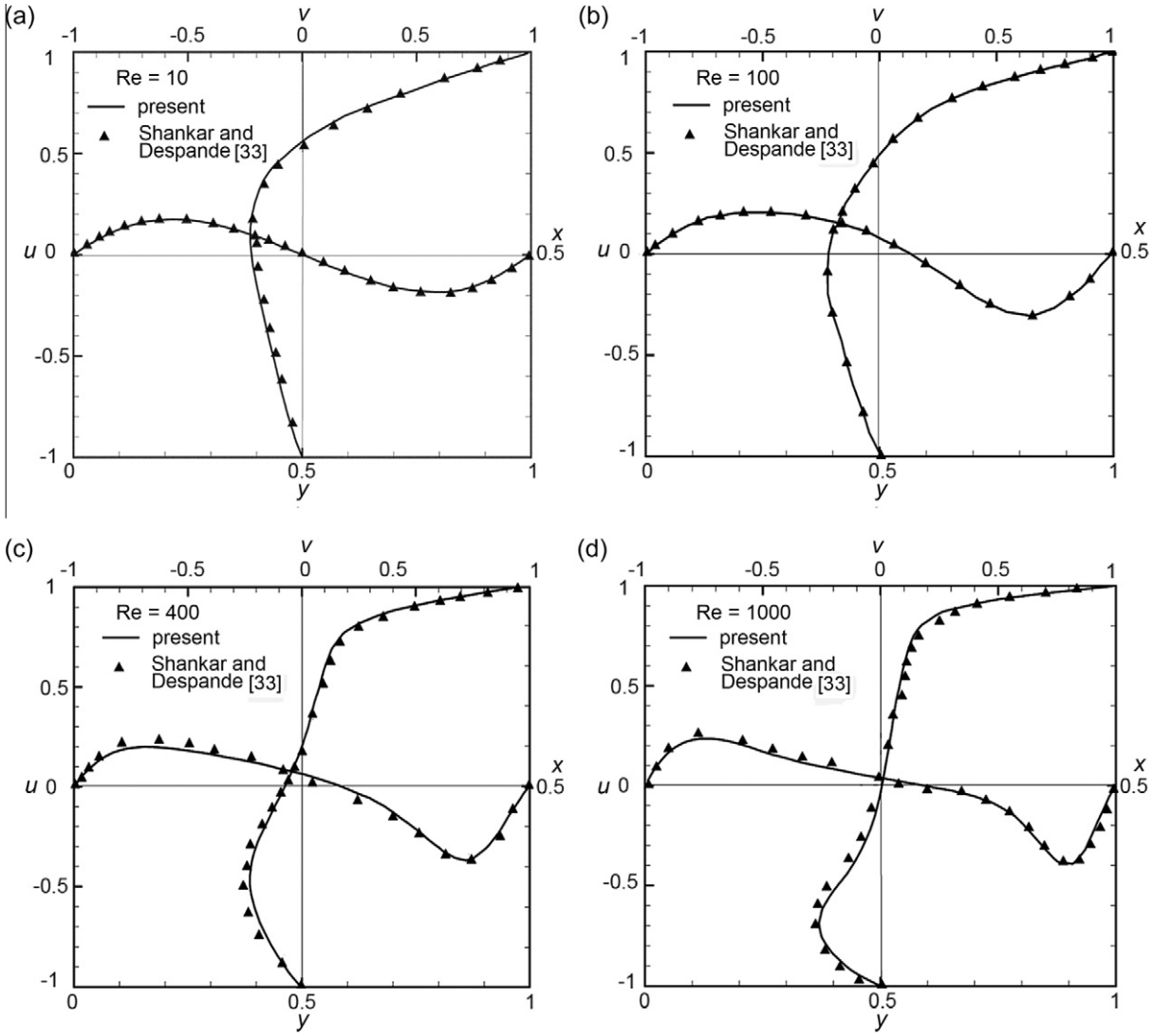

Fig. 5. Comparison of computed velocity profiles at the mid-sectional plane of a lid-driven three dimensional square cavity of unit span with Shankar and Deshpande [33] for various Reynolds numbers.

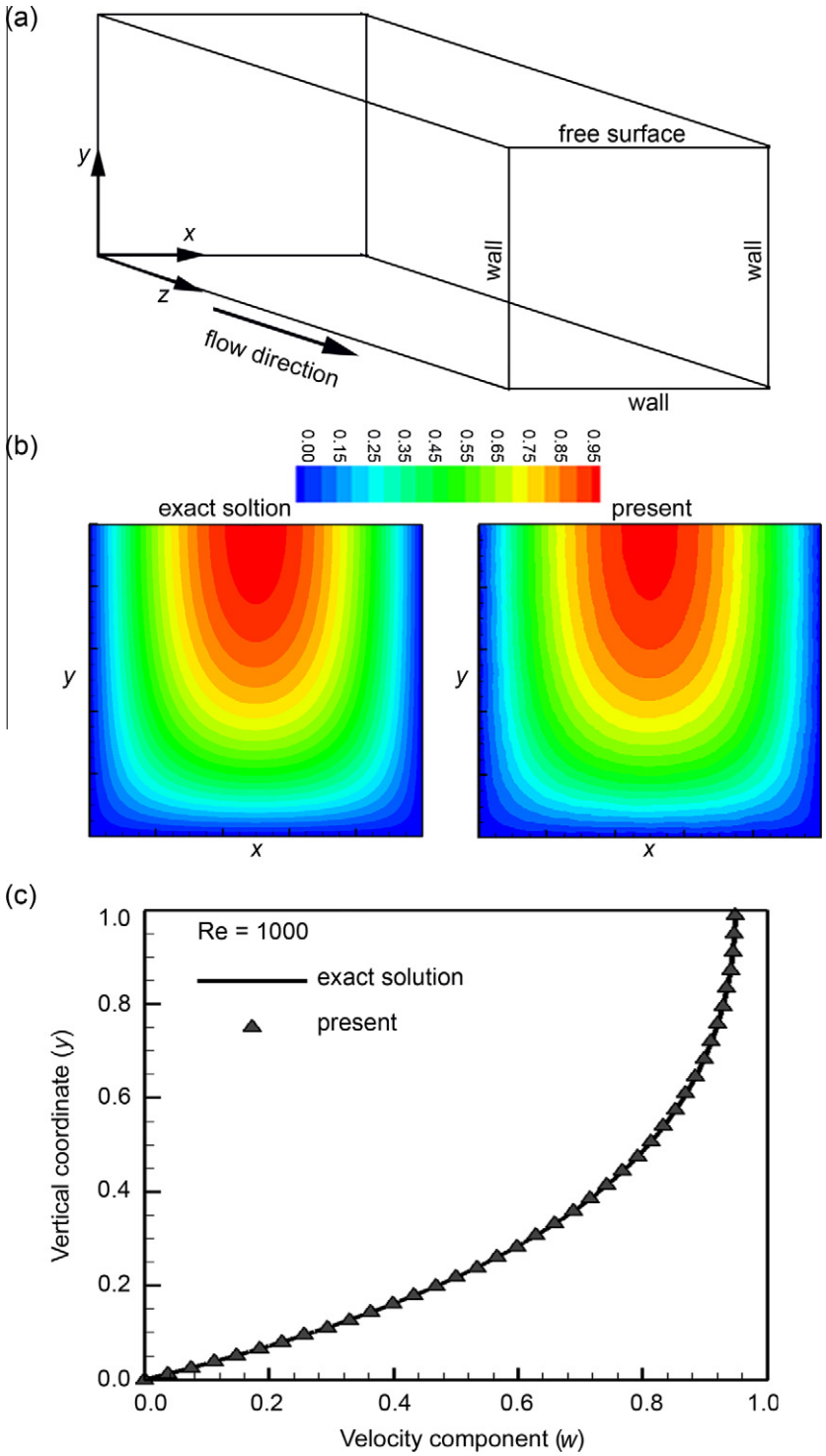

Fig. 6. Validation of the free surface boundary condition in fully developed open channel flow. (a) Computational domain and its boundary description. (b) u-velocity contour of exact solution of fully developed flow through an open channel compared with the numerical solution in x–y plane. (c) Velocity profile as a function of the vertical coordinate(y).

The discretized system of algebraic equations is solved by the stabilized bi-conjugate gradient method (biCGStab) with a diagonal pre-conditioner. The overall numerical algorithm used in the present study is quite similar to that presented by Date [29]. Points of difference are related to the use of certain invariant properties of the tetrahedral element and a powerful linear equations solver. Iterations within the code are executed till an absolute residual convergence criterion of $<10^{-7}$ for all the computing variables is achieved. The finite volume code is parallelized on shared memory architecture using the OpenMP model and all computations carried out on the high performance computing system available at IIT Kanpur (India).

3.1. Implementation of free surface boundary condition

Let a vector-quantity, such as velocity or a normal derivative at a boundary face, be denoted as $(\phi)_{fb}$. The general form of the free

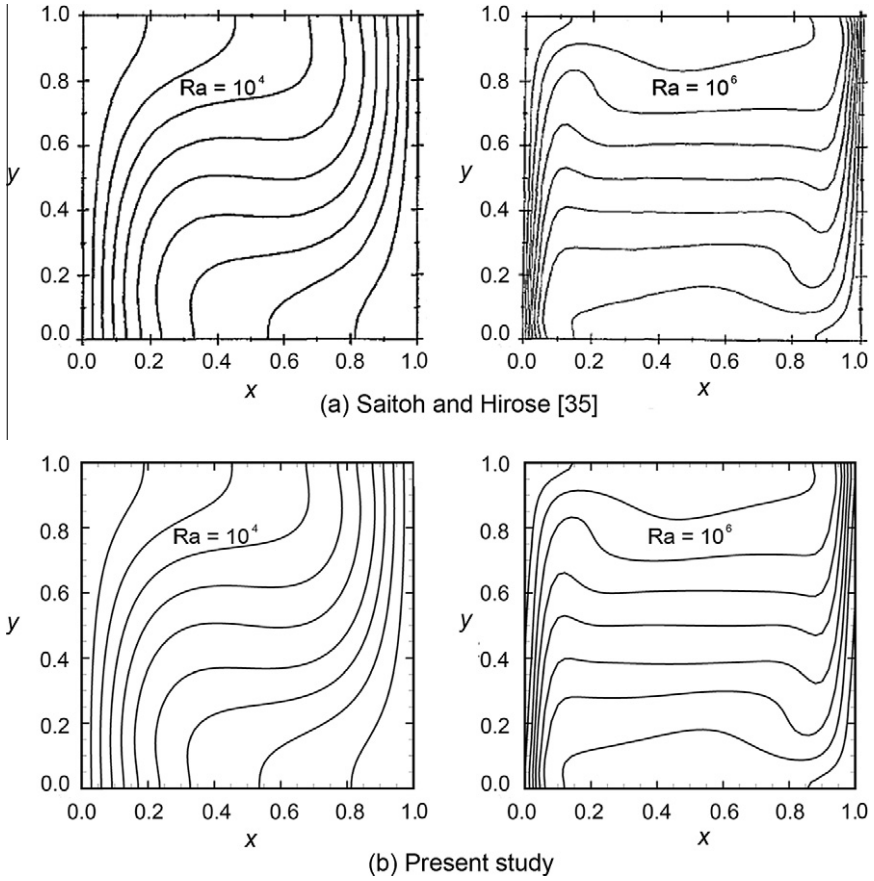

Fig. 7. Validation of the numerical simulation of the energy equation in terms of isotherms in a two dimensional lid driven cavity against Saitoh and Hirose [35] at various Rayleigh numbers. (a) Saitoh and Hirose [35] and (b) present study.

Table 1
Validation of the finite volume code for natural convection in a square cavity.

Heat transfer	$Ra = 10^4$, grid (50×50)		$Ra = 10^6$, grid (50×50)	
	Reference [35]	Present	Reference [35]	Present
$\overline{Nu}$	2.23850	2.23851	8.48430	8.48460
Nu_{max}	3.515580	3.515583	17.451	17.453
Nu_{min}	0.5864	0.5864	1.011	1.012

surface boundary conditions for variable ϕ in local curvilinear coordinates is given as:

$$(\phi_n)_{fb} = 0; \quad \left(\frac{\partial \phi_{t_1}}{\partial n}\right)_{fb} = 0; \quad \left(\frac{\partial \phi_{t_2}}{\partial n}\right)_{fb} = 0 \tag{8}$$

Here, n, t_1, and t_2 represent unit vectors in the normal and tangential directions over the face. The subscript fb represents the center of the boundary face and $\hat{i}, \hat{j}$, and $\hat{k}$ is unit vectors in the Cartesian coordinates, as shown in Fig. 2. The discretized forms of the free surface boundary condition, in local curvilinear coordinates, can be written as:

$$(\phi \cdot n)_{fb} = 0, \quad (\phi \cdot t_1)_{fb} = (\phi \cdot t_1)_{Cb} \text{ and } (\phi \cdot t_2)_{fb} = (\phi \cdot t_2)_{Cb} \tag{9}$$

Here, Cb represents a cell center of the free surface boundary tetrahedron as shown in Figs. 2 and 3. Since the governing equations are solved in Cartesian coordinates, free surface boundary conditions in curvilinear coordinates, as in Eqs. (8), (9) need to be transformed to Cartesian coordinates, with the derivatives evaluated for the Cartesian components of velocity. With $(\phi)_{fb}$ interpreted as velocity and subscripts indicating components, we have the following expressions:

$$(\phi)_{fb} = (\phi_x)_{fb}\hat{i} + (\phi_y)_{fb}\hat{j} + (\phi_z)_{fb}\hat{k} \tag{10}$$

$$(\phi)_{fb} = (\phi_n)_{fb}n + (\phi_{t_1})_{fb}t_1 + (\phi_{t_2})_{fb}t_2 \tag{11}$$

For the velocity vector, one can identify $u = \phi_x$, $v = \phi_y$, and $w = \phi_z$. The unit vectors in local curvilinear coordinates (n, t_1, t_2) can be calculated in terms of Cartesian unit vectors $(\hat{i}, \hat{j}, \hat{k})$ as follows. The area vector Δ enclosed by the triangular base with vertices $P_1(x_1, y_1, z_1)$, $P_2(x_2, y_2, z_2)$ and $P_3(x_3, y_3, z_3)$ (Fig. 2) is given as:

$$\Delta = \frac{1}{2}\begin{vmatrix} \hat{i} & \hat{j} & \hat{k} \\ x_2 - x_1 & y_2 - y_1 & z_2 - z_1 \\ x_3 - x_1 & y_3 - y_1 & z_3 - z_1 \end{vmatrix} \tag{12}$$

$$\text{Alternatively, } \Delta = A\hat{i} + B\hat{j} + C\hat{k} \tag{13}$$

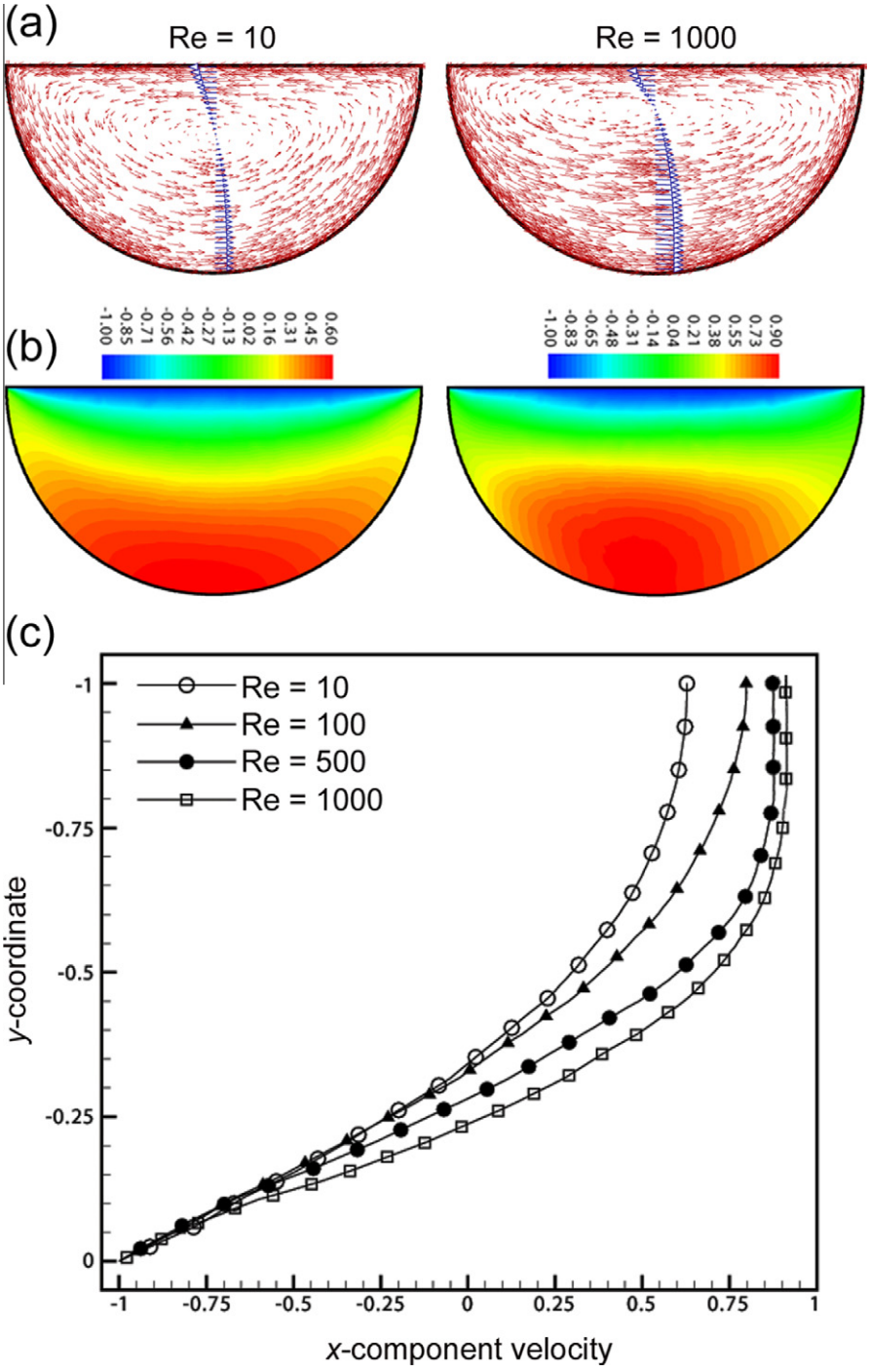

Fig. 8. Fluid flow pattern inside a pendant drop of contact angle 90° at Re = 10 and Re = 1000. (a) Velocity vectors (u and v) in red color and velocity component (u) in blue color at $x = 0$ and $z = 0$. (b) u velocity distribution over the frontal $z = 0$ plane on a color scale and (c) dimensionless u-velocity profile as a function of the vertical y-coordinate. (For interpretation of the references to colour in this figure legend, the reader is referred to the web version of this article.)

where,

$$\begin{aligned} A &= (y_2 - y_1) \times (z_3 - z_1) - (y_3 - y_1) \times (z_2 - z_1) \\ B &= (x_3 - x_1) \times (z_2 - z_1) - (x_2 - x_1) \times (z_3 - z_1) \\ C &= (x_2 - x_1) \times (y_3 - y_1) - (x_3 - x_1) \times (y_2 - y_1) \end{aligned} \tag{14}$$

The unit normal for the concerned area element is:

$$n = \frac{\Delta}{\|\Delta\|} \text{ which, in compact form, is } \quad n = A_1\hat{i} + B_1\hat{j} + C_1\hat{k} \tag{15}$$

The unit tangential vector (t_1) is assumed parallel to the one of triangle edges ($P_2 - P_1$) and is:

$$t_1 = \frac{(x_2 - x_1)\hat{i} + (y_2 - y_1)\hat{j} + (z_2 - z_1)\hat{k}}{\sqrt{(x_2 - x_1)^2 + (y_2 - y_1)^2 + (z_2 - z_1)^2}} \quad \text{or}$$

$$t_1 = A_2\hat{i} + B_2\hat{j} + C_2\hat{k}$$

The second unit tangential vector (t_2) is determined by the cross product of the unit normal (n) and the unit tangent (t_1), as:

$$t_2 = n \times t_1 = \begin{vmatrix} \hat{i} & \hat{j} & \hat{k} \\ A_1 & B_1 & C_1 \\ A_2 & B_2 & C_2 \end{vmatrix} \quad \text{or} \quad t_2 = A_3\hat{i} + B_3\hat{j} + C_3\hat{k} \tag{17}$$

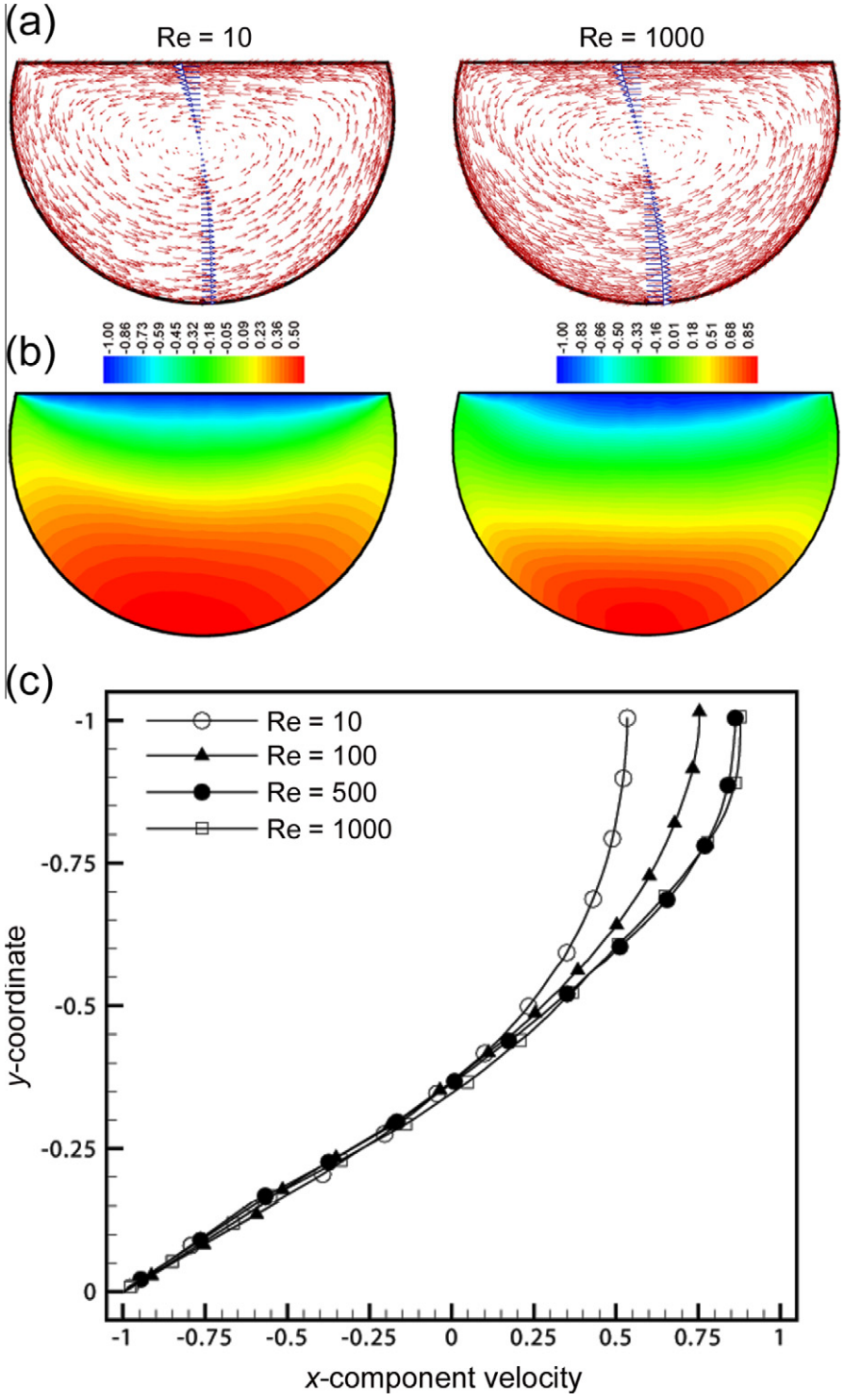

Fig. 9. Fluid flow pattern inside a pendant drop of contact angle 105° at Re = 10 and Re = 1000. (a) Velocity vectors (u and v) in red color and velocity component (u) in blue color at $x = 0$ and $z = 0$. (b) u velocity distribution over the frontal $z = 0$ plane on a color scale and (c) dimensionless u-velocity profile as a function of the vertical y-coordinate. (For interpretation of the references to colour in this figure legend, the reader is referred to the web version of this article.)

Substituting Eqs. (10) and (15)–(17) into Eq. (9), the free surface boundary conditions relating the boundary value (*fb*) to an interior value (*Cb*) are obtained as:

$$(\phi_x)_{fb}A_1 + (\phi_y)_{fb}B_1 + (\phi_z)_{fb}C_1 = 0 \tag{18}$$

$$(\phi_x)_{fb}A_2 + (\phi_y)_{fb}B_2 + (\phi_z)_{fb}C_2 = (\phi_x)_{Cb}A_2 + (\phi_y)_{Cb}B_2 + (\phi_z)_{Cb}C_2 \tag{19}$$

$$(\phi_x)_{fb}A_3 + (\phi_y)_{fb}B_3 + (\phi_z)_{fb}C_3 = (\phi_x)_{Cb}A_3 + (\phi_y)_{Cb}B_3 + (\phi_z)_{Cb}C_3 \tag{20}$$

These three equations can be solved for the face-centered variables given by the subscript *fb* in terms of cell-centered quantities (*Cb*).

3.2. Calculation of friction coefficient and heat transfer coefficient

Navier-Stokes and energy equations are solved with appropriate boundary conditions over the physical domain of the drop. Once the field variables $[\phi = (u, v, w, p, T)]$ have converged, velocity and temperature gradients are calculated for determining the skin

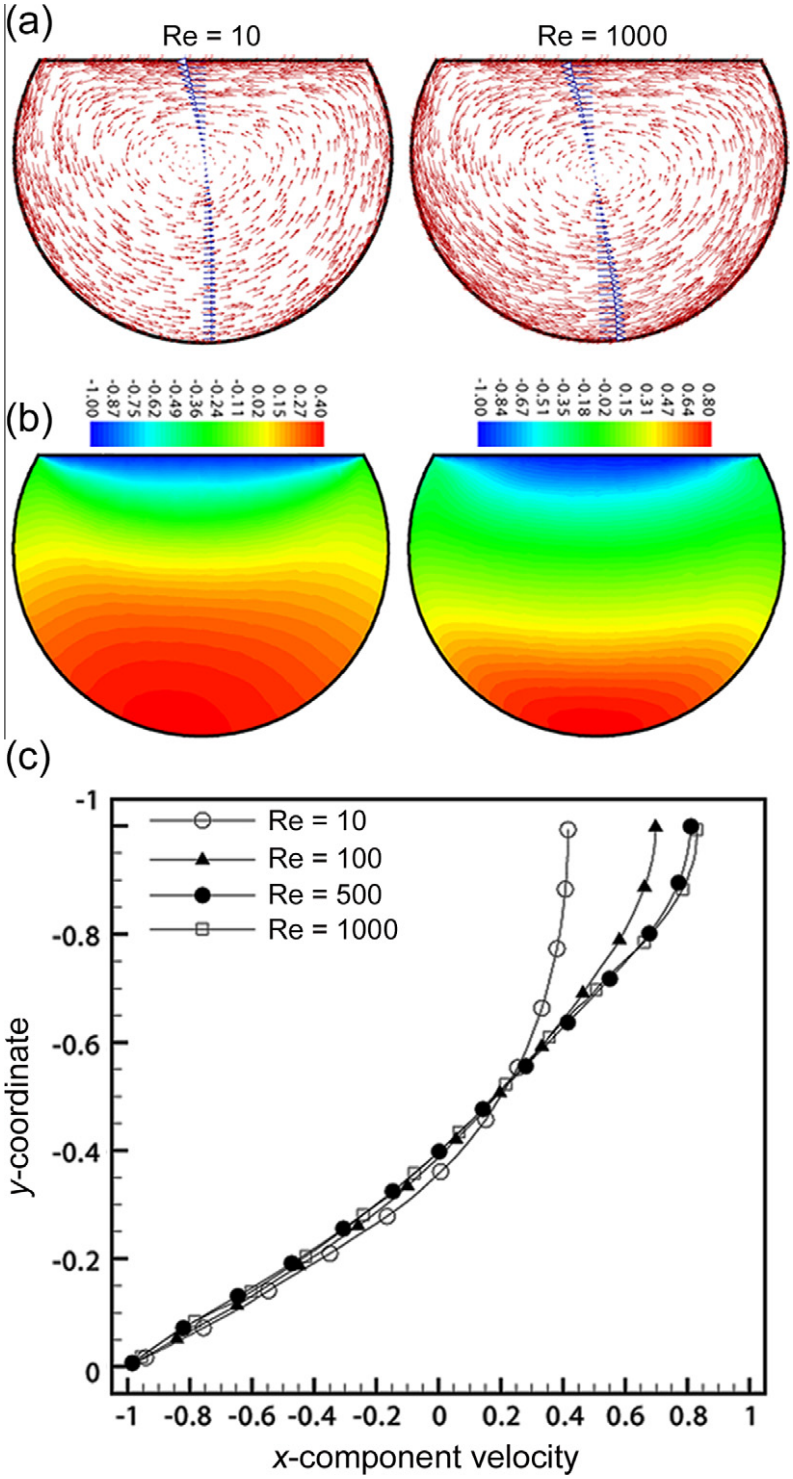

Fig. 10. Fluid flow pattern inside a pendant drop of contact angle 120° at Re = 10 and Re = 1000. (a) Velocity vectors (u and v) in red color and velocity component (u) in blue color at $x = 0$ and $z = 0$. (b) u velocity distribution over the frontal $z = 0$ plane on a color scale and (c) dimensionless u-velocity profile as a function of the vertical y-coordinate. (For interpretation of the references to colour in this figure legend, the reader is referred to the web version of this article.)

friction coefficient and heat transfer coefficient, as per Eqs. (6) and (7). Gradients of velocity components (u, v and w) near the wall with respect to the x, y and z directions are computed as follows. For a generic variable (ϕ) the Cartesian derivatives are approximated as:

$$\left(\frac{\partial\phi}{\partial x}\right)_f = \left(\frac{\phi_{fbx} - \phi_{cbx}}{d_{cfx}}\right); \quad \left(\frac{\partial\phi}{\partial y}\right)_f = \left(\frac{\phi_{fby} - \phi_{cby}}{d_{cfy}}\right); \quad \left(\frac{\partial\phi}{\partial y}\right)_z = \left(\frac{\phi_{fbz} - \phi_{cbz}}{d_{cfz}}\right) \tag{21}$$

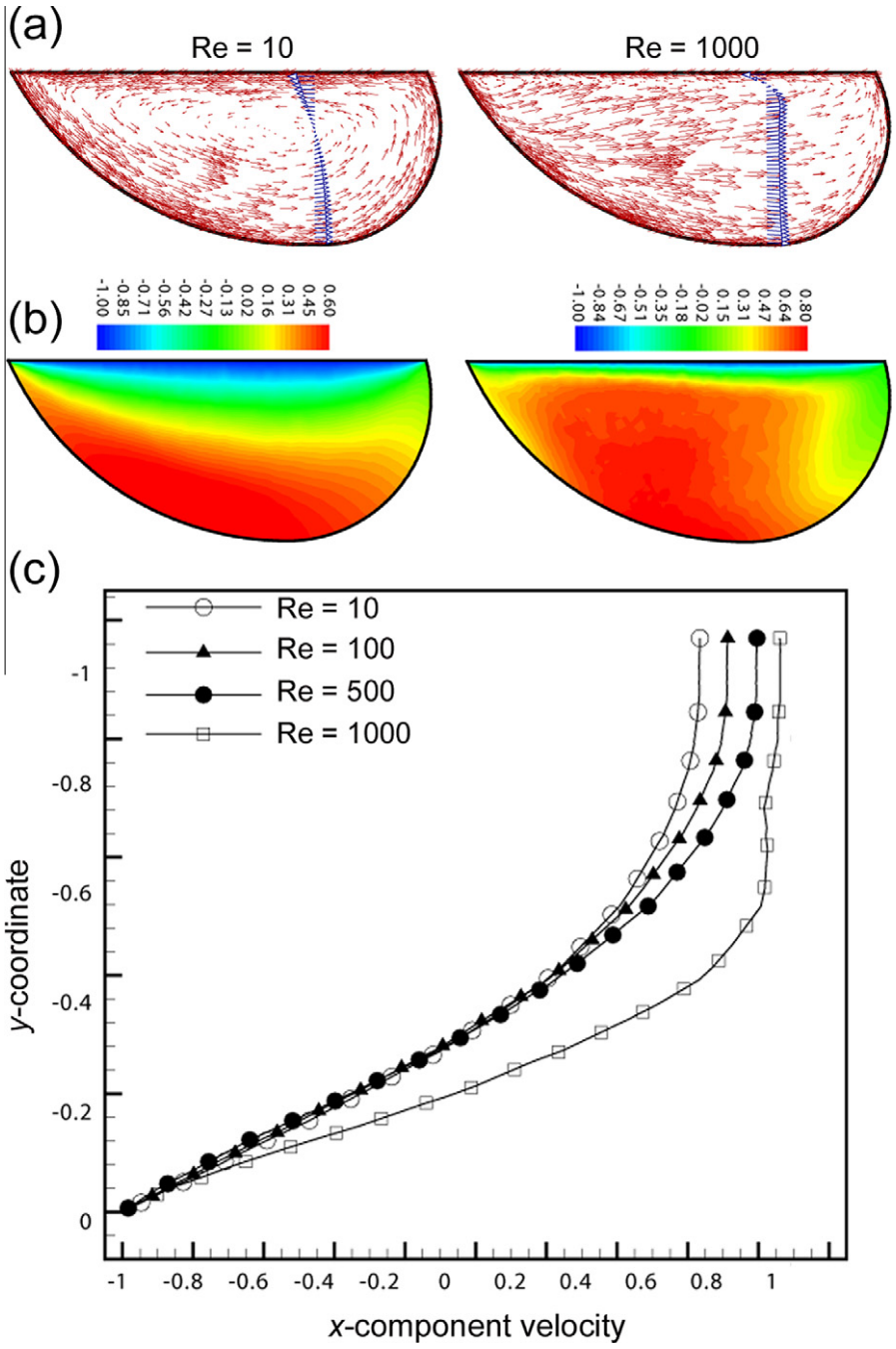

Fig. 11. Fluid flow pattern inside a deformed pendant drop of contact angles 55° and 105° at Re = 10 and Re = 1000. (a) Velocity vectors (u and v) in red color and velocity component (u) in blue color at $x = 0$ and $z = 0$. (b) u velocity distribution over the frontal $z = 0$ plane on a color scale and (c) dimensionless u-velocity profile as a function of the vertical y-coordinate. (For interpretation of the references to colour in this figure legend, the reader is referred to the web version of this article.)

For calculation of the local heat transfer coefficient, the normal gradient of temperature near the wall is calculated as:

$$\left(\frac{\partial\phi}{\partial n}\right)_f = \left(\frac{\phi_{fb} - \phi_{cb}}{d_{cf}}\right) \tag{22}$$

Here, d_{cfx}, d_{cfy} and d_{cfz} are distances between the cell center and the center of the face overlapping the wall in the appropriate coordinate direction, while d_{cf} is the total distance between the cell center and the center of the face overlapping the wall. For high quality grids, this segment and the wall normal direction happen to be identical; this inherently assures high accuracy in gradient calculations.

With the derivatives calculated from Eqs. (21) and (22), the local wall shear stress and heat transfer coefficient are obtained from Eqs. (6) and (7). Let $(\tau_w)_i$ be the local shear stress at each face of the base of the drop. In addition, $(A_f)_i$ is area of the ith face and there are N such faces over the wall. The average shear stress at the wall is calculated as:

$$\overline{\tau_{wall}} = \frac{\sum_{i=1}^{N}(\tau_{wall})_i (A_f)_i}{\sum_{i=1}^{N}(A_f)_i} \tag{23}$$

The average skin friction coefficient is determined as:

$$\overline{C}_f = \frac{\overline{\tau_{wall}}}{\frac{1}{2}\rho U^2} \tag{24}$$

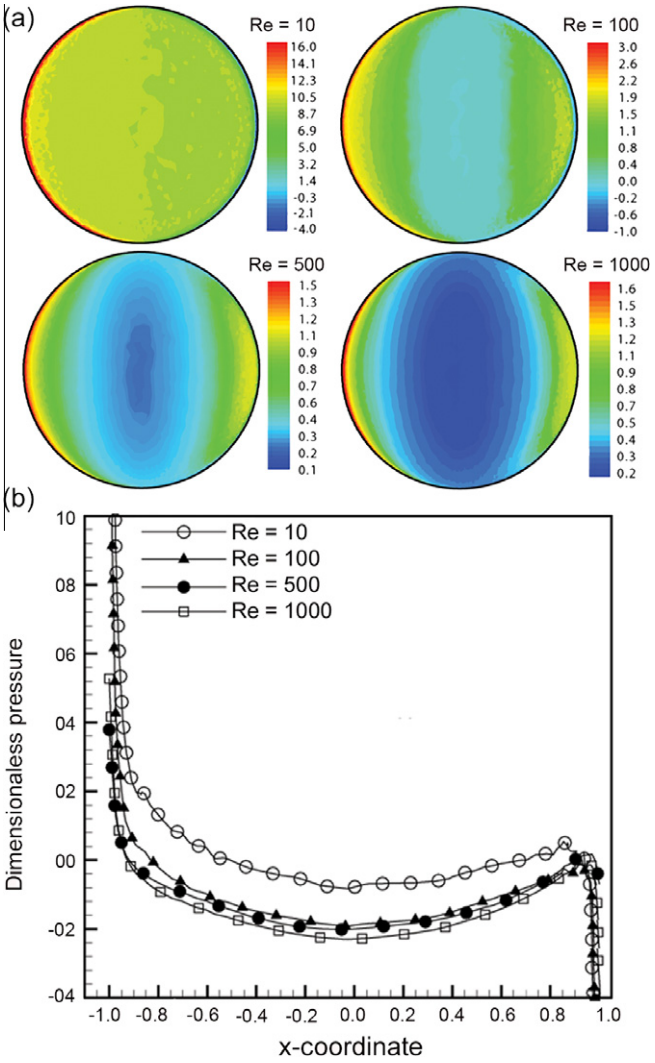

Fig. 12. (a) Wall pressure distribution at the base of a pendant drop of contact angle 90° and Re = 10, 100, 500 and 1000. (b) Variation of non-dimensional pressure with respect to the *x*-direction that is aligned with the direction of motion of the surface.

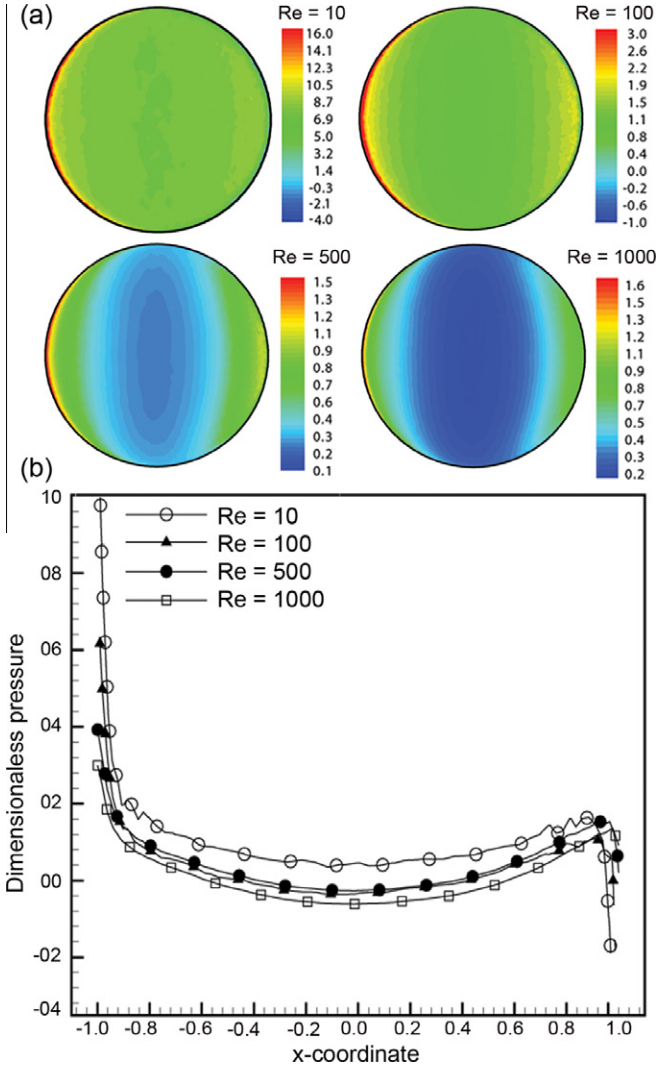

Fig. 13. (a) Wall pressure distribution at the base of a pendant drop of contact angle 105° and Re = 10, 100, 500 and 1000. (b) Variation of non-dimensional pressure with respect to the *x*-direction that is aligned with the direction of motion of the surface.

With the local heat flux at the *i*th face of the wall given as $(q_{wall})_i$ (Eqs. (7) and (22)), the average heat flux is calculated as:

$$\overline{q_{wall}} = \frac{\sum_{i=1}^{N}(q_{wall})_i(A_f)_i}{\sum_{i=1}^{N}(A_f)_i} \tag{25}$$

The average heat transfer and the corresponding Nusselt number at the wall are determined as:

$$\left.\begin{aligned} \bar{h} &= \frac{\overline{q_{wall}}}{(T_{free} - T_{wall})} \\ \overline{\mathrm{Nu}} &= \frac{\bar{h}d}{k} \end{aligned}\right\} \tag{26}$$

4. Grid independence and code validation

To examine if the solutions obtained were grid independent, numerical experiments were performed with 5,84,000, 9,84,234, 12,43,560 and 14,44,345 tetrahedral elements at the highest Reynolds number (=2500), Prandtl number of 5.8 and for a symmetric liquid drop of contact angle, 105°. The *u* velocity component and temperature variation with respect to the vertical *y*-coordinate over the frontal *x*–*y* plane ($z = 0$) are shown in Fig. 4(a) and (b), respectively. It is seen that identical results are obtained for 12,43,560 and 14,44,345 cells. Hence, a grid with 12,43,560 cells was chosen for further computations. Similar results were obtained for drops of other shapes as well.

For validation of the Navier–Stokes solver, its predictions were compared against benchmark results available for a three-dimensional lid driven cavity [33] at various Reynolds numbers. The comparison is shown in Fig. 5. The computed results of the present study are in good agreement with the benchmark solution available in the literature.

The free surface boundary condition was validated by considering fully developed flow in a channel of square cross-section whose top surface is open to the atmosphere. The description of the physical domain is shown in Fig. 6(a). The boundary condition at the inlet plane is taken to be uniform in the initial calculations and the velocity profiles obtained at the outlet plane are used in subsequent computations over the inflow plane. Pressure over the free surface of the outlet plane is taken to be zero. No-slip conditions are applied at the side and lower walls, while the top surface is given free surface conditions. The solution is obtained by solving the governing equations in three dimensions at a Reynolds number of 1000. The analytical solution for the geometry considered is given below [34]:

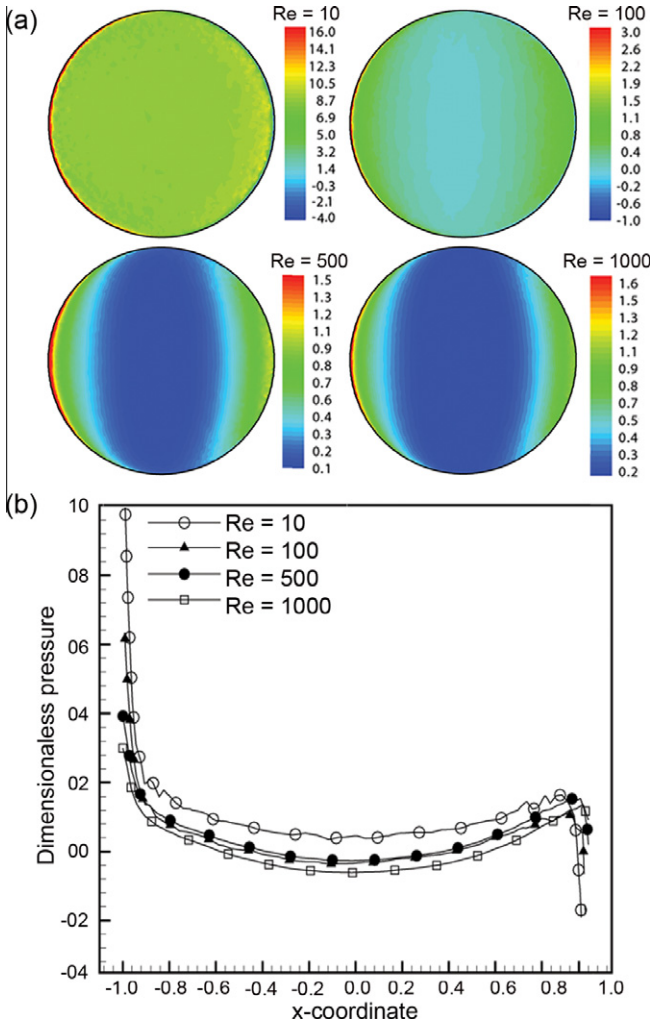

Fig. 14. (a) Wall pressure distribution at the base of a pendant drop of contact angle 120° and Re = 10, 100, 500 and 1000. (b) Variation of non-dimensional pressure with respect to the x-direction that is aligned with the direction of motion of the surface.

$$w(x,y) = \sum_{m=1}^{\infty}\sum_{n=1}^{\infty} A_{mn}\sin(m\pi x)\cdot\sin\left(\frac{(2n-1)\pi y}{2}\right) - B_{mn} = \frac{\int_0^1\int_0^1 \sin(m\pi x)\sin\left(\frac{(2n-1)\pi y}{2}\right)dxdy}{\int_0^1\int_0^1 \sin^2(m\pi x)\sin^2\left(\frac{(2n-1)\pi y}{2}\right)dxdy} \quad (27)$$

where,

$$A_{mn} = \frac{-B_{mn}}{(m\pi)^2+\left(\left(\frac{2n-1}{2}\right)\pi\right)^2}$$

Fig. 6(b) shows the contours of the axial velocity component obtained from the exact solution and compared with the computer code of the present study. Fig. 6(c) shows the velocity profiles obtained from Eq. (27) as well as the numerical simulator. The comparison is seen to be quite favorable.

The finite volume code has been validated for Navier–Stokes and energy equations jointly by considering natural convection heat transfer in a heated two dimensional cavity [35]. The horizontal walls are differentially heated while the top and bottom surfaces are adiabatic. Rayleigh numbers considered are 10^4 and 10^6, Prandtl number is 0.71, and simulation has been carried out with a grid of 50×50 triangular cells. The comparison of the present study with [35] in terms of isotherms and streamlines is shown in Fig. 7. The comparison is found to be quite good. The minimum, maximum, and the average Nusselt numbers are compared in Table 1. The quantitative comparison is seen to be excellent.

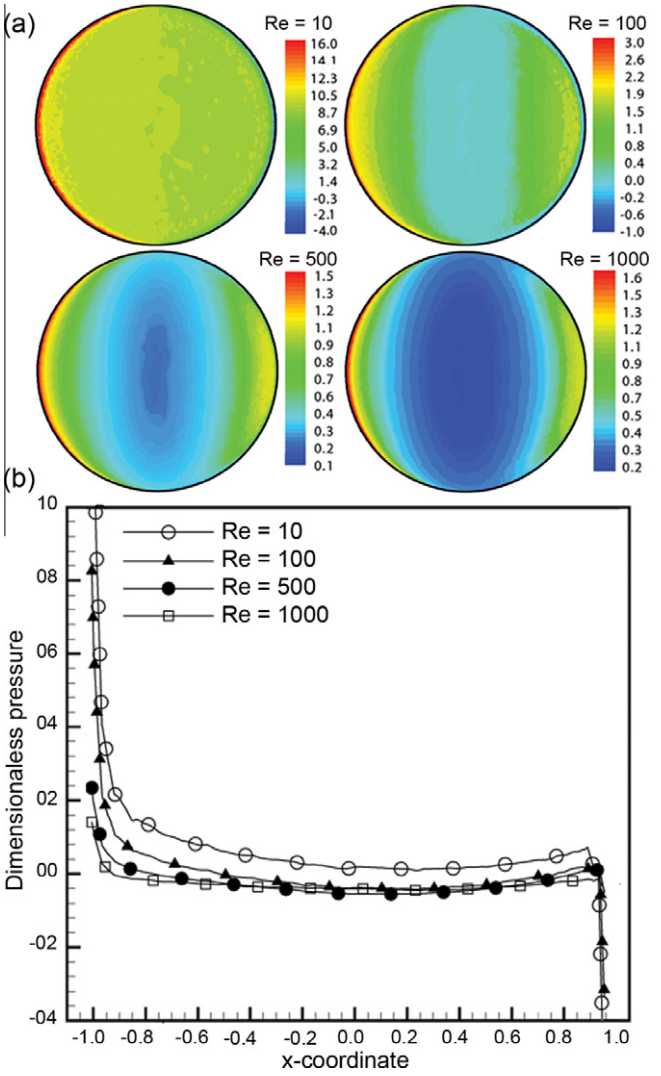

Fig. 15. (a) Wall pressure distribution at the base of a deformed pendant drop of contact angles 55° and 105° and Re = 10,100, 500 and 1000. (b) Variation of non-dimensional pressure with respect to the x-direction that is aligned with the direction of motion of the surface.

5. Results and discussion

To understand fluid flow and heat transfer within the pendant liquid drop, computed predictions are displayed in the form of velocity vectors, velocity profiles, wall pressure distribution, wall shear stress, profiles of dimensionless temperature and wall heat transfer rates. As stated earlier, the drop is taken to be stationary, while the surface is given a constant velocity. As the present study is related to dropwise condensation, vectors and contours have been shown for a drop in the pendant position with respect to the surface. The range of parameters considered is: Reynolds number (Re) = 10–1000 and Prandtl number (Pr) = 0.005 to 30. Symmetric drops with apparent contact angles of 90°–120° and a deformed drop with advancing and receding angles of 105° and 55° have been studied. Since the flow and thermal fields are three-dimensional, contours have been presented on the frontal x–y plane ($z = 0$), the wall, namely the x–z plane ($y = 0$) and the cross-sectional plane normal to the plane of the paper, namely the y–z plane ($x = 0$), Fig. 2(b). The average wall shear stress and average wall heat flux are expressed in the form of correlations.

Results have been presented for drops of equal volumes. For a given drop volume, the contact area of drop on the substrate wall

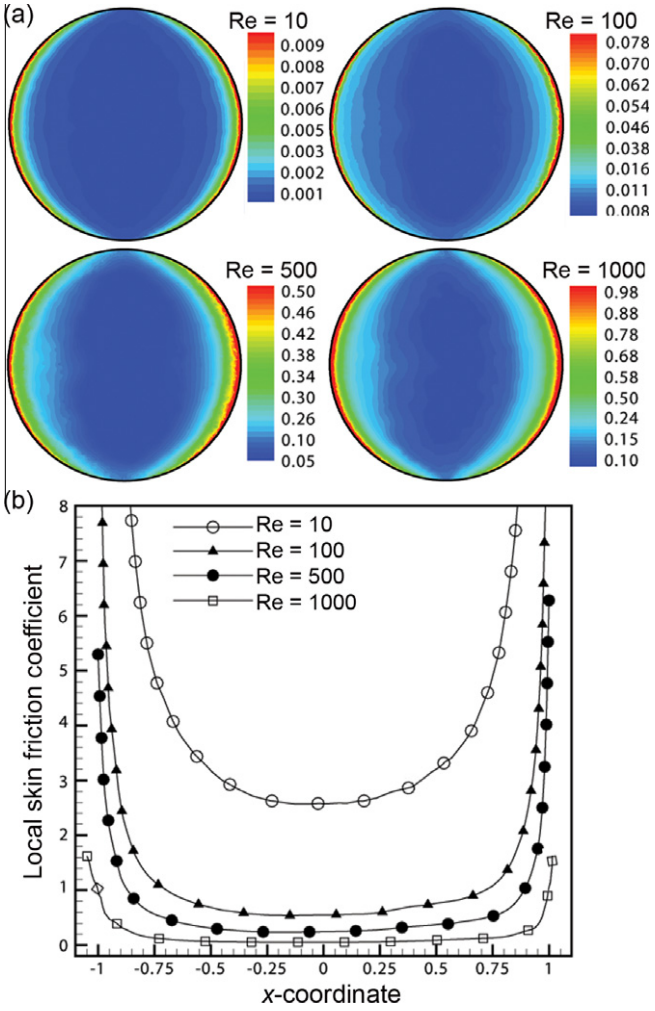

Fig. 16. (a) Local wall shear stress distribution at the base of a pendant drop of contact angle 90° at Re = 10, 100, 500 and 1000. (b) Variation of local skin friction coefficient with respect to the *x*-direction that is aligned with the direction of motion of the surface.

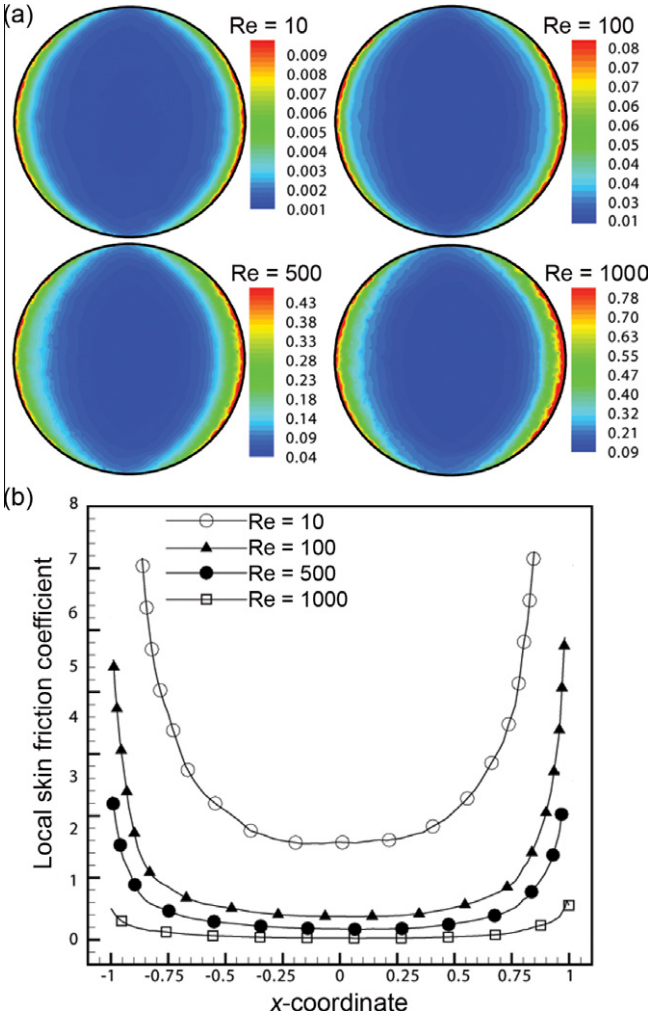

Fig. 17. (a) Local wall shear stress distribution at the base of a pendant drop of contact angle 105° at Re = 10, 100, 500 and 1000. (b) Variation of local skin friction coefficient with respect to the *x*-direction that is aligned with the direction of motion of the surface.

and hence, its base diameter decreases as the apparent contact angle increases. Similarly, the maximum vertical extent of the drop measured from the solid surface increases with increasing contact angle for symmetric drops. The deformed drop has a larger base diameter and a smaller vertical height. As the base diameter of the drop is used as a length scale in the simulations, results have been presented for unit base diameter and the vertical extent (normal distance between the droplet-base and the free surface) is a free parameter, depending on the contact angle. Similarly, the imposed velocity to the substrate is the chosen scale and is shown by vectors of equal length in the figures. In dimensionless form, the wall and free surface temperatures are zero and unity, respectively.

5.1. Velocity field and wall pressure distribution

Flow patterns inside three-dimensional drops of various shapes are shown in Figs. 8–11. Figs. 8–11 (a) show velocity vectors and the profile of the *x*-velocity component with respect to vertical coordinate passing through the center of the drop. The plane on which the vectors have been shown is the frontal (*x*–*y*) plane, where $z = 0$ and wall movement is from right to left. Vectors are drawn in terms of the *x* and *y* components of velocity. As expected, fluid is mobilized at the solid surface and goes around along the free surface, forming a circulation pattern. The velocity vectors are skewed for a deformed drop, particularly at the highest Reynolds number. The velocity vectors in Figs. 8–11(a) agree well with published experimental data [26] and the smooth particle hydrodynamics estimations [28] for symmetric drops.

The *x*-component velocity changes direction in the interior of the drop. At low Reynolds number, the point of zero velocity is closer to the center and the circulation pattern is approximately symmetrical. With increasing Reynolds number, the location inside the drop where the *x*-component velocity changes sign shifts towards the base of the drop ($y = 0$). This effect is most prominent at Re = 1000. The movement of the point of zero *x*-velocity with Reynolds number inside the drop is clearly seen in Fig. 8(c) for an apparent contact angle of 90°. It is less visible at 105° and 120°, but is quite prominent for the deformed drop.

Magnitude of *x*-component velocity is shown in Figs. 8–11(b) as color distribution. With increasing Reynolds number, the zone near the interface, located farthest from the substrate, attains a large but oppositely directed velocity (with respect to the imposed substrate velocity), whose magnitude approaches unity with increasing Reynolds number. As a portion of the fluid is mobilized at high speeds, the average speed of fluid particles in the core is simultaneously lower. The *x*-component velocity variation with respect to the vertical coordinate is shown in Figs. 8–11(c) for various Reynolds numbers and drop shapes. The graphs show that

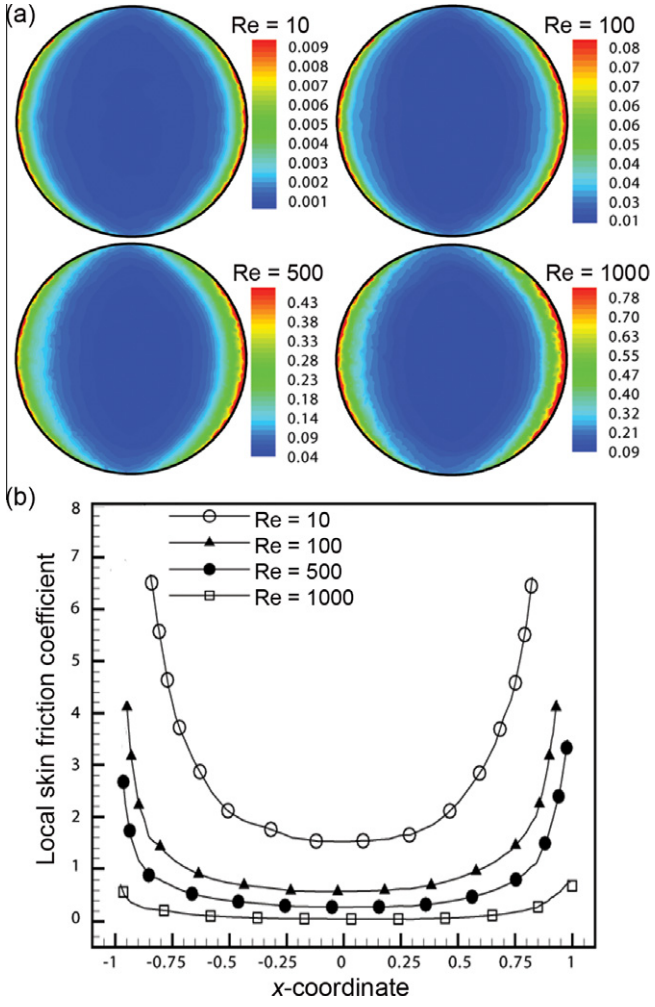

Fig. 18. (a) Local wall shear stress distribution at the base of a pendant drop of contact angle 120° at Re = 10, 100, 500 and 1000. (b) Variation of local skin friction coefficient with respect to the x-direction that is aligned with the direction of motion of the surface.

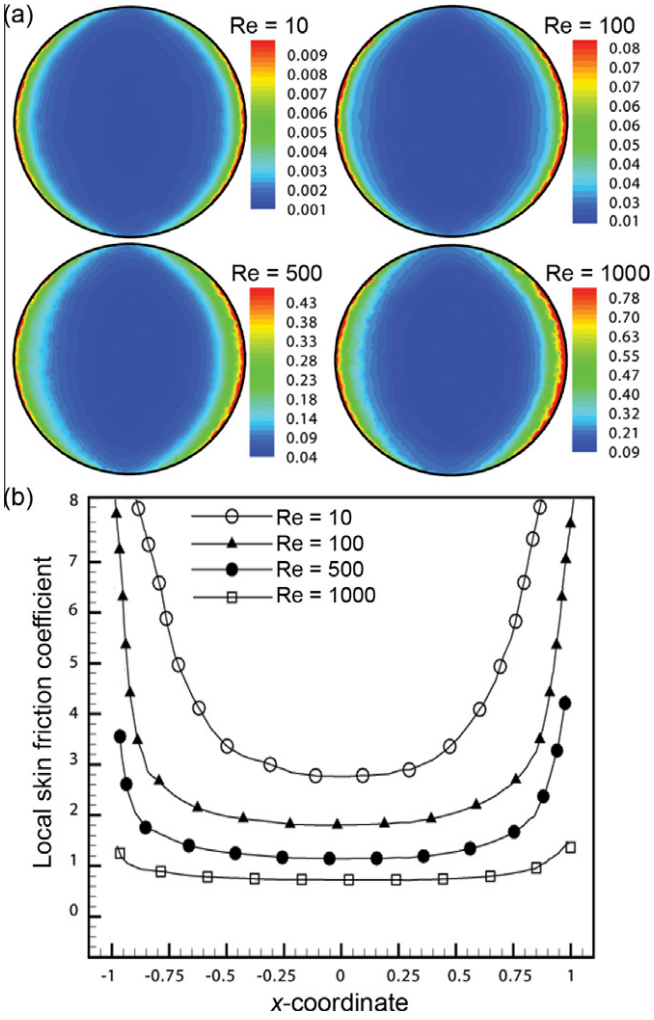

Fig. 19. (a) Local wall shear stress distribution at the base of a deformed drop of contact angles 55° and 105° at Re = 10, 100, 500 and 1000. (b) Variation of local skin friction coefficient with respect to the x-direction that is aligned with the direction of motion of the surface.

the u-velocity variation is linear closer to the wall. For symmetric drops, the wall velocity gradient along the central axis is nearly independent of Reynolds number. The slope, however, depends on the contact angle. For a deformed drop, the central axis is not having symmetry and stronger Reynolds number effects are to be seen in near-wall velocity profile and the gradients thereof. The free surface velocity gradient is zero in two orthogonal tangential directions, as imposed by the stress-free boundary conditions.

The dimensionless wall pressure distribution, as a function of contact angle, for the symmetric drops and deformed drops is shown in Figs. 12–15 for Reynolds number of 10, 100, 500 and 1000. As pressure is scaled by $\frac{1}{2}\rho U^2$, the changes in pressure are inversely related to Re, being smaller at higher Reynolds numbers. The wall pressure distributions are qualitatively similar in the figures shown. The central portion of the droplet base has a near-constant pressure; the constant value decreasing with increasing Reynolds number. These results are realized for the deformed drop as well. Large changes in pressure are visible around the periphery. The wall pressures are constant and close to zero in the core region while the free surface pressure is the datum for pressure calculations. Under these circumstances, it can be concluded that much of the shape of the drop would remain unaffected by the motion of the surface. The wall pressure increases around the left boundary, the direction in which the surface is given motion. The other

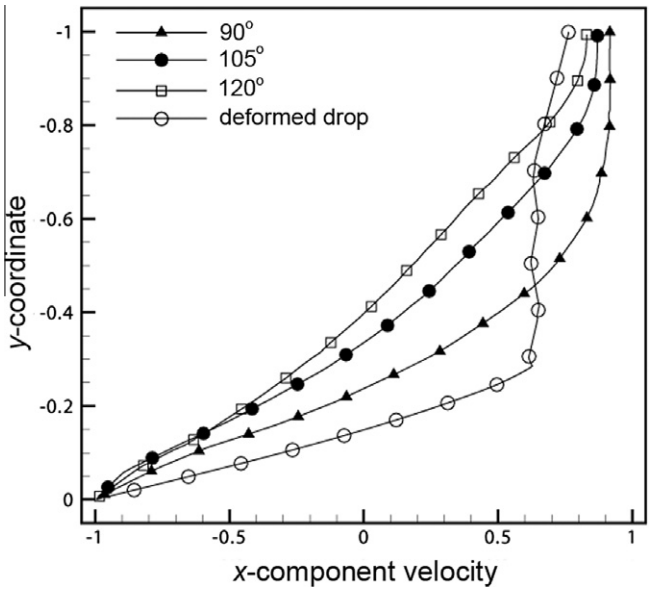

Fig. 20. Effect of contact angle on the x-component velocity profile along the vertical coordinate on the x–y plane ($z = 0$) at Re = 1000.

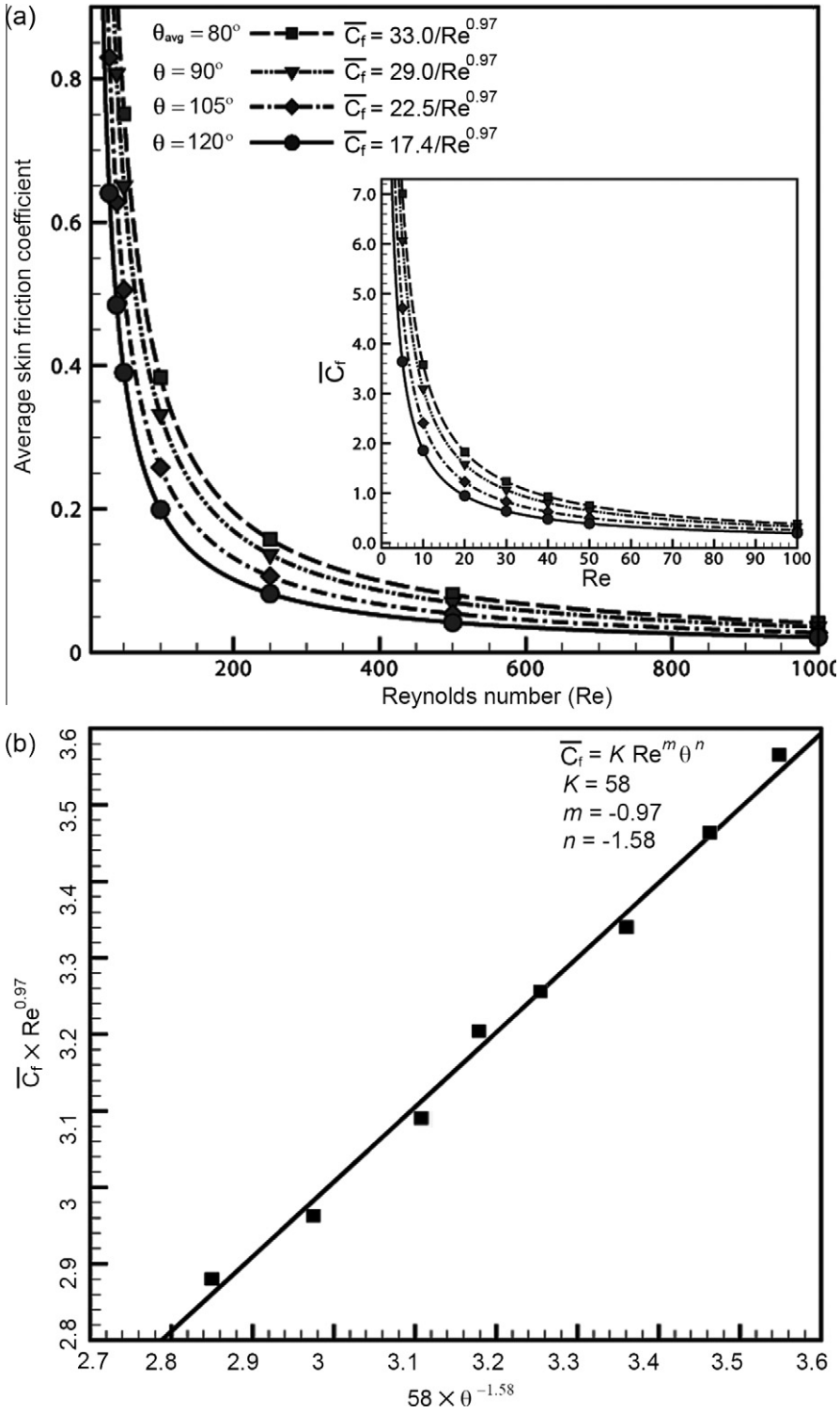

Fig. 21. (a) Skin friction coefficient C_f as a function of Reynolds number. Inset shows data for small Reynolds numbers. (b) Parity plot of $\log(C_f \times \mathrm{Re}^{0.97})$ with respect to $\log(58 \times \theta^{-1.58})$.

side experiences a lowering of pressure (Figs. 12–15(b)). These changes are Reynolds number dependent, being sharper at higher Reynolds numbers. In a real liquid drop, the local pressure changes would be accommodated by slight alterations in the drop shape, so as to satisfy the Young-Laplace condition.

The distributions of respective local wall shear stress contours, in terms of the skin friction coefficient, are shown in Figs. 16–19. The Reynolds number range considered is 10 to 1000 while three symmetric and one deformed drop geometries are studied. Analogous to pressure, the skin friction coefficient is scaled by $\frac{1}{2}\rho U^2$ and its magnitude scales inversely as Reynolds number. Wall shear stresses are small and constant in the central region of the droplet base, decreasing though with increasing Reynolds numbers. For symmetric drops, this variation is symmetric indicating a corresponding symmetric flow-pattern circulation. The fluid turns in the region close to the contact line to conform to the shape of

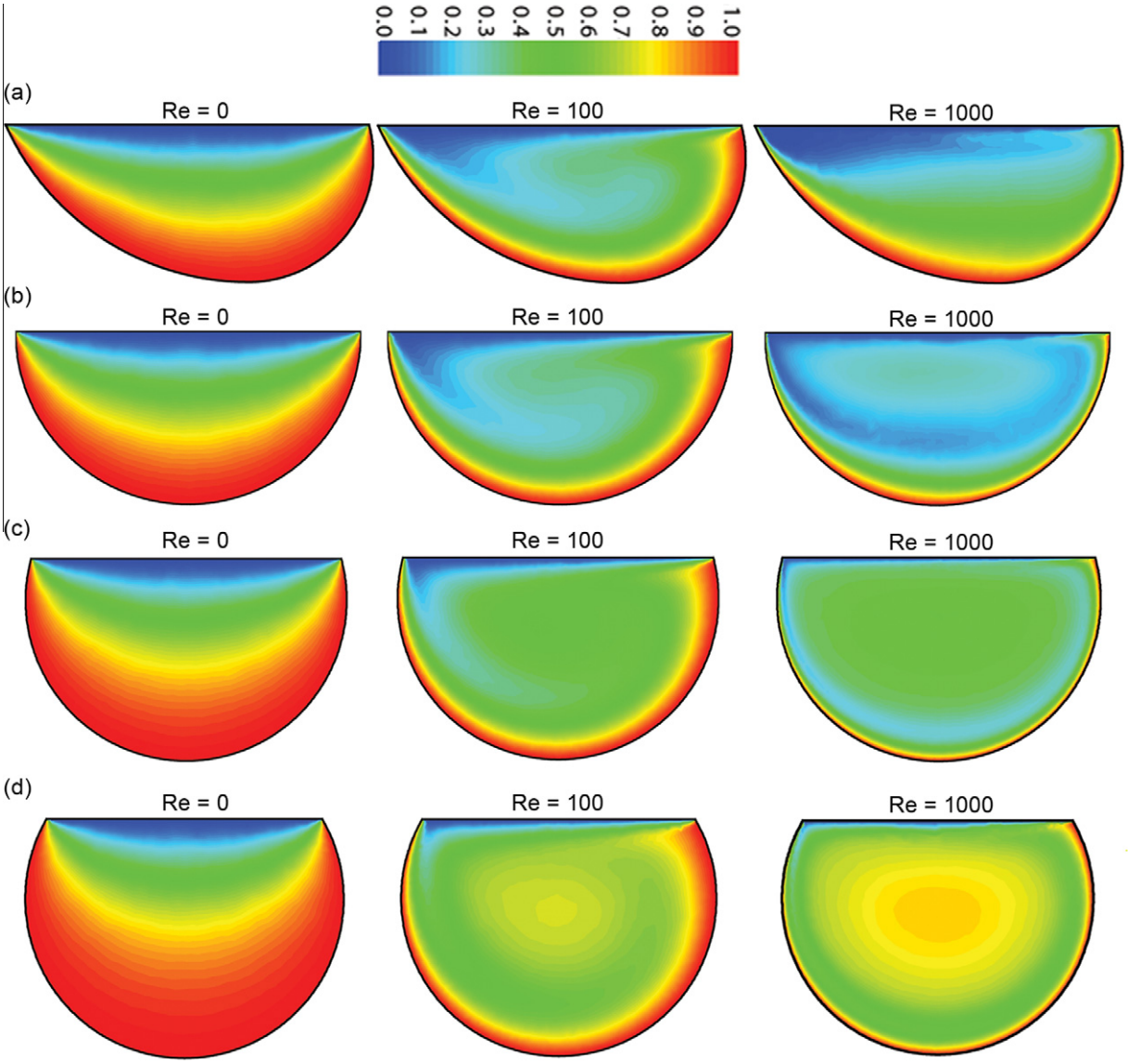

Fig. 22. Temperature field inside drops of various shapes at Pr = 6 as a function of Reynolds number. (a) Deformed drop with a receding angle of 55° and an advancing angle of 105°; (b) symmetric drop whose contact angle is 90°; (c) contact angle, 105°; and (d) contact angle, 120°. Re = 0 represents the conduction limit.

the drop; this region is prone therefore to high shear rates, an observation also recorded by many other researchers (for example,[13] and [14]). The effect of loss of symmetry in a deformed drop is barely visible in the shear stress profiles. However, the deformed drop encounters greater wall shear stress as compared to the symmetric drop at all Reynolds numbers. Overall, the sensitivity of skin friction coefficient to change in drop shape (deformation) is stronger than that of change in Reynolds number.

To highlight the effect of the drop shape on wall shear stress, the *x*-component velocity is plotted, as a function of the vertical coordinate in Fig. 20. Among the symmetric drops, the wall velocity gradient is the highest for drop with 90 °Contact angle and the lowest for the one with 120°. Thus, increasing hydrophobicity has a clear effect of lowering wall shear stress. This effect can be explained by noting that turning motion of the fluid in droplets of higher apparent contact is more gradual, thereby creating a smaller obstruction to the internal flow and thus, milder gradients thereof. Fig. 20 also shows that the wall shear stress for a deformed drop is considerably greater, for the choice of the advancing and receding angles considered. These trends are realized in the local skin friction coefficient profiles of Figs. 16–19.

5.1.1. Average skin friction coefficient

The average skin friction coefficient is determined from Eqs. (23) and (24) by averaging shear stresses over the entire base of the drop, including the edges. The pressure variation at the wall shows constancy in pressure over large central portions of the base, excluding the region close to the contact line. This trend suggests that the near-wall flow is akin to a flat plate boundary-layer with a skin friction coefficient scaling of $Re^{-1/2}$. On the other hand, wall shear stresses are also nearly constant over the base of the drop, suggesting a situation closer to laminar, fully developed channel flow behavior, with a scaling of Re^{-1}. To examine the scaling of skin friction coefficient with Reynolds number and apparent contact angle, the numerical data was fitted with a power law of the form

$$\overline{C_f} = CRe^{a}$$

for each contact angle and,

$$\overline{C_f} = KRe^{m}\theta^{n}$$

for all Reynolds numbers and contact angles. Here, θ in radians is the contact angle for symmetric drops, and the average of

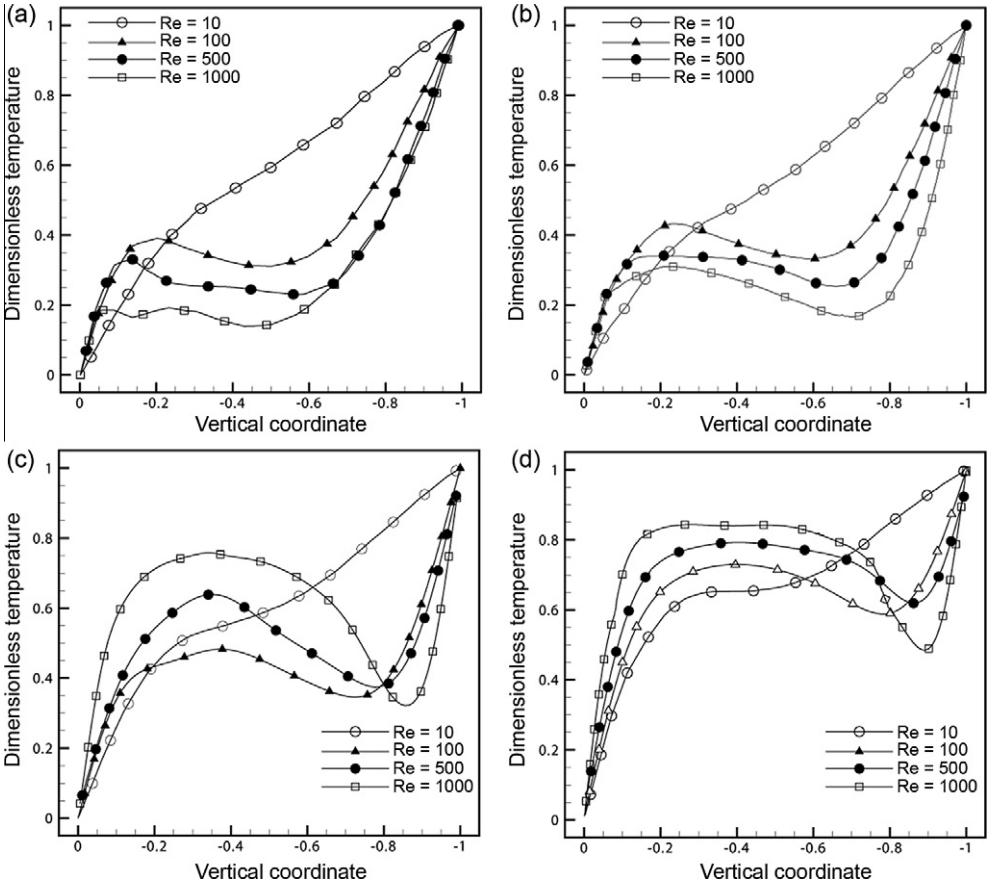

Fig. 23. Non-dimensional temperature profile along the vertical coordinate over the x–y plane ($z = 0$) at Pr = 6 and for various Reynolds numbers. (a) Deformed drop with advancing and receding angles of 105 and 55°; (b) contact angle 90° (c) contact angle 105° and (d) contact angle 120°.

advancing and receding angles for a deformed drop, as per the case. Fig. 21(a) is a plot of the numerical data showing the variation of the skin friction coefficient with Reynolds number for each contact angle. Fig. 21(b) is a parity plot between the best fit obtained by regression and the numerical data from finite volume calculations. The quality of regression is seen to be quite good. For each contact angle, a correlation is obtained as:

$$\begin{aligned}
&\theta = 90^{\circ} \Rightarrow \overline{C_f} = 29\mathrm{Re}^{-0.97} \\
&\theta = 105^{\circ} \Rightarrow \overline{C_f} = 22.5\mathrm{Re}^{-0.97} \\
&\theta = 120^{\circ} \Rightarrow \overline{C_f} = 17.4\mathrm{Re}^{-0.97} \\
&\theta = 80^{\circ}\,(\theta_{adv} = 105^{\circ}, \theta_{rcd} = 55^{\circ} \text{ for deformed}) \Rightarrow \overline{C_f} = 33\mathrm{Re}^{-0.97}
\end{aligned} \tag{28}$$

These correlations show that the skin friction coefficient increases as the contact angle decreases. The skin friction coefficient of a deformed drop is considerably higher. The dependence on Reynolds number is closer to a reciprocal relationship indicating channel flow behavior. The correlation that includes apparent contact angle as a variable is derived from numerical data as:

$$\overline{C_f} = 58\mathrm{Re}^{-0.97}\theta^{-1.58} \tag{29}$$

Here, the skin friction coefficient shows a strong dependence on θ (in radians), being higher for smaller values of contact angle. Eqs. (28) and (29) contain the overall impact of fluid motion within the drop in the form of shear stress acting over the solid surface.

5.2. Temperature distribution

The dimensionless temperature field in the liquid drop, on a color scale is presented in Fig. 22. The free surface is at temperature unity while the wall temperature is zero. For definiteness, Prandtl number is kept at a value of 6. A Reynolds number of zero indicates the conduction limit when the fluid velocities are zero. Data for Re = 0, 100 and 1000 are presented. At the conduction limit, temperature spreads uniformly over the drop cross-section. At higher Reynolds numbers, a circulation pattern is formed and the temperature gradients at the two surfaces, i.e., free surface and wall of drop, are greatly enhanced. These gradients are not equal because of differences in areas across which heat transfer takes place at the wall and the free surface. Thermal boundary layers are visible near the isothermal surfaces across which large temperature changes take place, temperature gradients near the free surface being lower because of a higher surface area. Hence, the thermal boundary-layer thickness (shown in red) is greater than the corresponding variation at the solid wall (shown in blue). The patch of blue seen on the left side of each drop is indicative of cold fluid transported by the surface velocity. The spread in color is related to fluid turning at the forward corner. The core of the fluid in the drop shows minor changes in color and is closer to isothermal. At the highest Reynolds number, thermal boundary-layers are uniformly thin for symmetric drops. For the deformed drop, the thermal boundary-layer near the free surface continues to be thick because of the nature of the flow field set up. Here, the point of zero velocity is considerably closer to the wall and a near-flat velocity variation is obtained near the flat surface. Thus, transverse velocities are

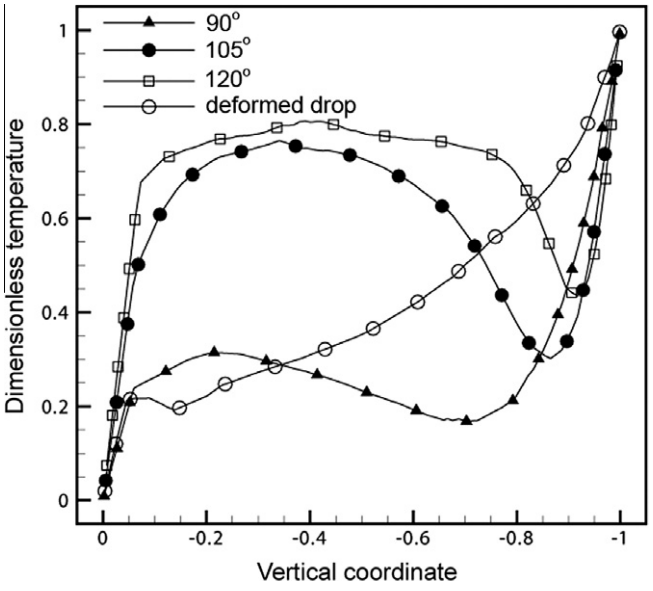

Fig. 24. Effect of contact angle on the non-dimensional temperature profile along the vertical coordinate over the x-y plane ($z = 0$) at Re = 1000 and Pr = 6.

small and heat transfer from the free surface of the fluid to the drop interior has a diffusional component. The corresponding thermal gradients are smaller and the color plot shows a red patch of definite thickness near the free surface.

Temperature profiles across the drop are shown as a function of Reynolds number, for symmetric and deformed drops, in Fig. 23. Prandtl number is again kept at a value of 6. At the lowest Reynolds number, diffusion is an important mode of heat transfer and temperature varies almost linearly across the drop height. Larger temperature gradients are clearly visible near the wall and the free surface at higher Reynolds numbers. For symmetric drops, these gradients continuously increase with Reynolds number. In the core of the fluid, temperature shows an inversion, with a temperature peak on the cold side and temperature minimum on the hot side. Temperature constancy in the core is best seen in a drop of apparent contact angle 120°. For the deformed drop, the change in temperature gradient with increasing Reynolds is consistently observed at the solid surface but is less evident near the free surface. This is because of the shift in the fluid circulation pattern towards the solid surface that prevents fluid velocities from becoming large even when Reynolds number is increased from 500 to 1000.

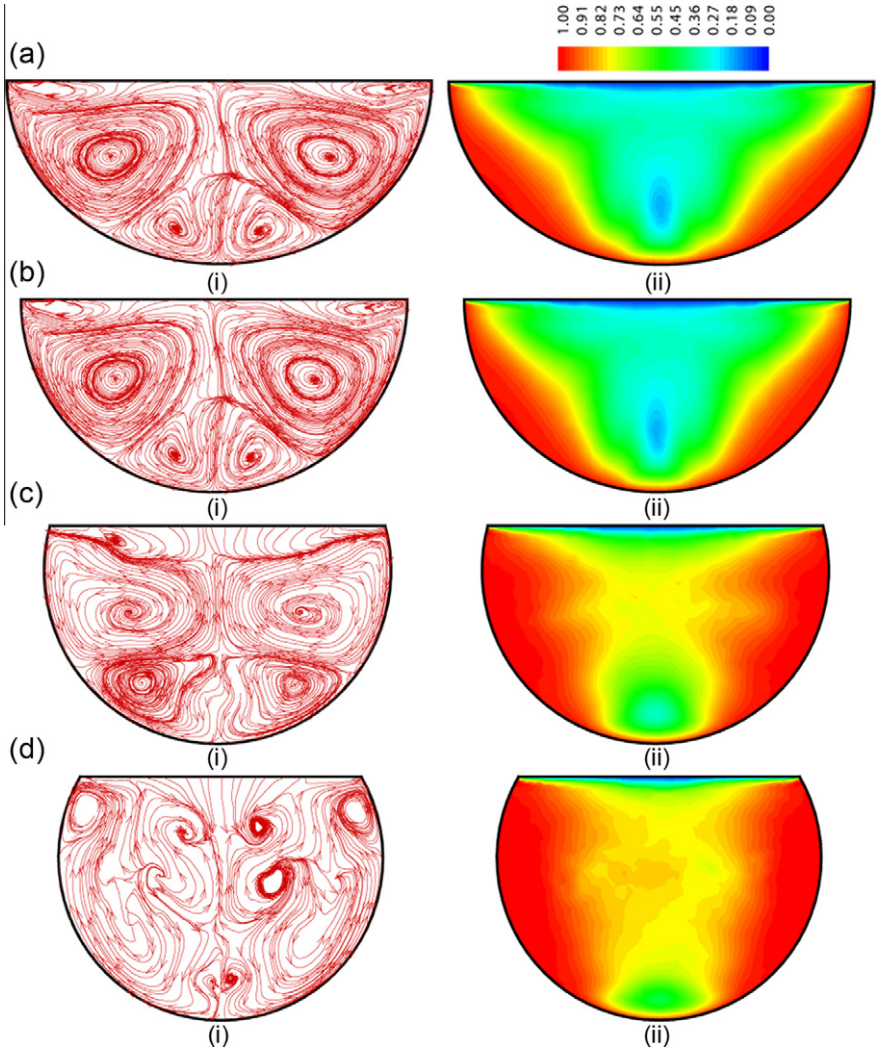

Fig. 25. Streamlines (left) and temperature distribution (right) on a cross plane(y–z plane at $x = 0$) for (a) deformed drop of contact angles 105° and 55° respectively, and, symmetric drops of contact angles (b) 90° (c) 105° and (d) 120° respectively; all cases at Pr = 6 and Re = 1000.

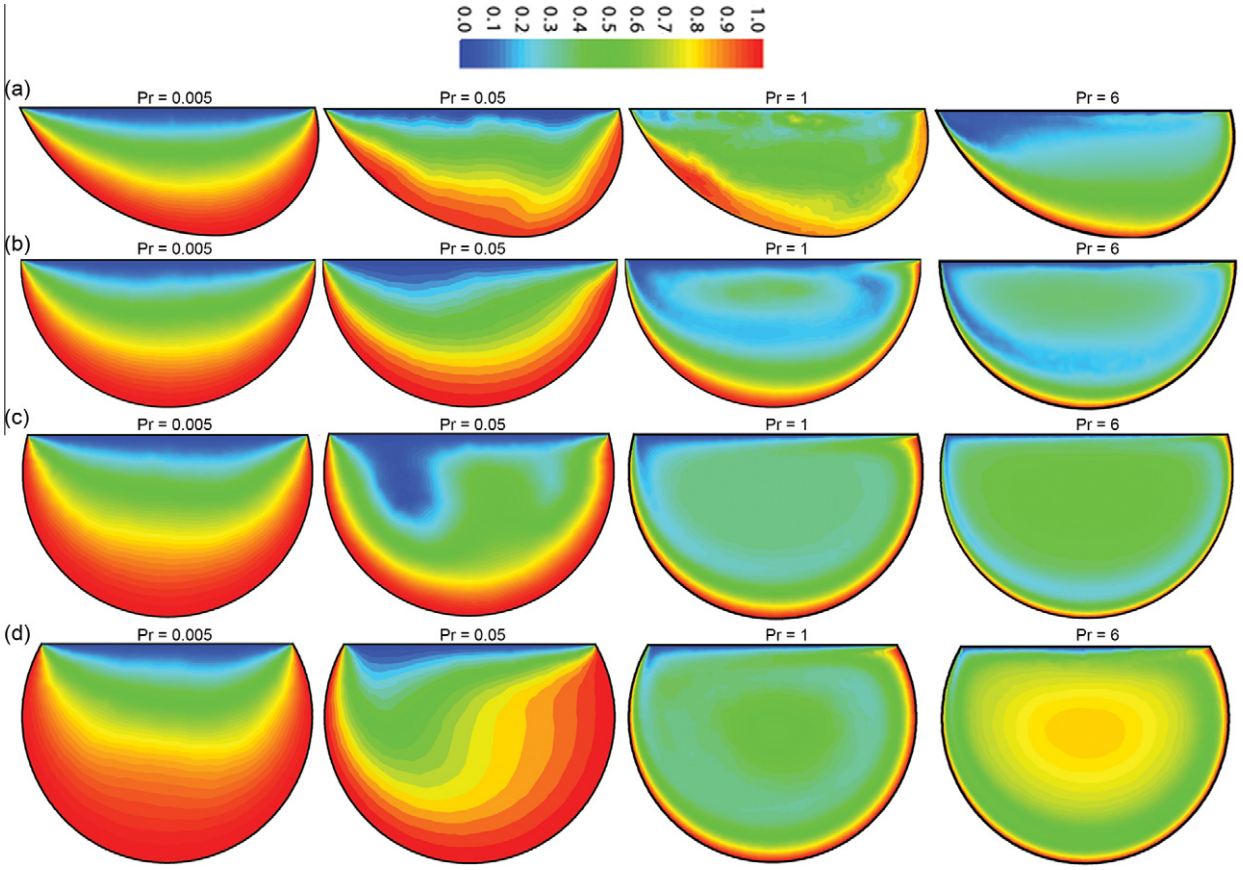

Fig. 26. Temperature fields inside drops of various shapes at Re = 1000 and for a range of Prandtl numbers. Contact angles are (a) 90° (b) 105° (c) 120°and (d) deformed drop (105, 55°).

The effect of shape of the drop on temperature profile is presented in Fig. 24. Reynolds number considered is 1000 while Pr = 6. Large changes in temperature are to be seen near the wall ($y = 0$) and near the free surface ($y = -1$). All the three symmetric drops show near constancy of temperature in the core. This is because of the regularity of flow pattern in these geometries. For a deformed drop, an effective core is not formed within it (Fig. 11(a)). The recirculation pattern shifts towards the left corner and a body of slow moving fluid fills the drop elsewhere. A second factor is the smaller vertical extent of deformed drop compared to the symmetric drop. This factor influences temperature distribution in the interior. Jointly, a diffusion-like variation of temperature is seen in the central region. For the same reason, wall temperature gradient in a deformed drop is somewhat lower than those obtained for the symmetric geometries.

At high Reynolds numbers (Re > 100), Figs. 23 and 24 show inversion in temperature in the sense that temperature variation is not monotonic. This result can be explained in terms of the three dimensionality of the flow field created in the physical domain. Fig. 25 shows stream traces on a cross-plane of the drop along with temperature distribution on a color scale. The secondary flow is quite strong and exhibits a certain level of symmetry. This secondary flow enhances the mixing of the hot fluid near the droplet interface with the colder fluid near the wall region and vice versa.

5.2.1. Effect of Prandtl number

Prandtl number is the ratio of the kinematic viscosity of the fluid and thermal diffusivity. Liquids such as water have Pr > 1 while for liquid metals, thermal diffusivity is large and Pr is considerably smaller than unity. Fig. 26 shows isotherms in drops of various shapes at Re = 1000 for Pr = 0.005, 0.05, 1 and 6. For Pr > 1, flow is convection dominated and thermal boundary layers form adjacent to the hot and the cold surfaces. The core of the drop shows smaller temperature changes, though secondary flow may be important in creating non-monotonic trends in temperature. For Pr = 0.05 and 0.005, Fig. 26 shows that temperature gradients are smaller and temperature spreads evenly over the drop volume. Isotherms at Pr = 0.05 appear to follow the velocity vectors and the effect of convection is visible. However, at Pr = 0.005, conduction is the dominant mode of heat transfer and color contours appear closer to those of Re = 0 in Fig. 22. Here, wall temperature gradients would have become independent of Reynolds number.

5.2.2. Heat transfer rates

Figs. 27–30 show the distribution of the local wall heat transfer coefficient, in terms of Nusselt number, for various Reynolds numbers. Prandtl number is kept at 6 in these simulations. It is seen that the Nusselt number is nearly constant over the central core of the droplet base, with a value that increases with Reynolds number. Larger gradients, and hence Nusselt numbers, are attained around the drop periphery. These trends are visible in the line plots of Nusselt number plotted along the base of the drop (Figs. 27–30(b)). In these plots, flow is from right to left. Since the fluid particles have clockwise circulation, comparatively cold fluid reaches the wall on the right side as against the left. Hence, the local Nusselt numbers on the right side are considerably higher. Though the flow pattern in a deformed drop is skewed, when compared to the symmetric drops, the Nusselt number profiles show close similarity among the shapes considered.

Since the heat transfer rates for low Prandtl number fluids are quite different from those with higher Pr, results are presented in two parts: one for Pr > 1 (Fig. 31) and another for Pr < 0.3 (Fig. 32).

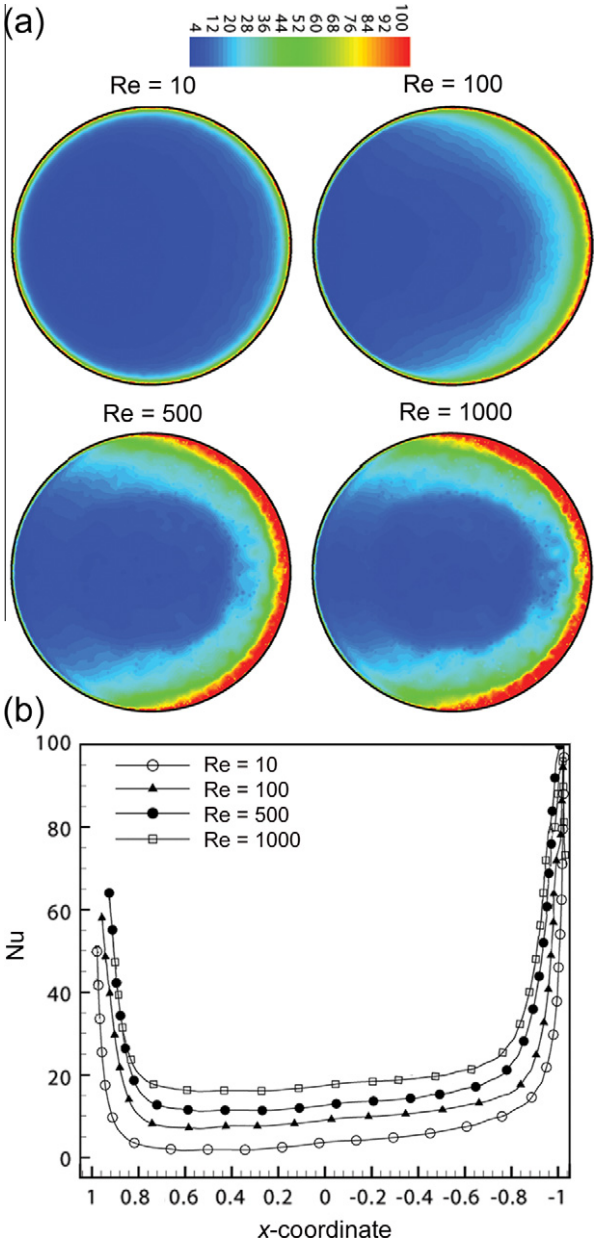

Fig. 27. Effect of Reynolds number: (a) Local Nusselt number distribution at the base of the drop of contact angle 90° and Pr = 6. (b) Variation of local Nusselt number as function of the *x*-coordinate that is aligned with the direction of surface motion.

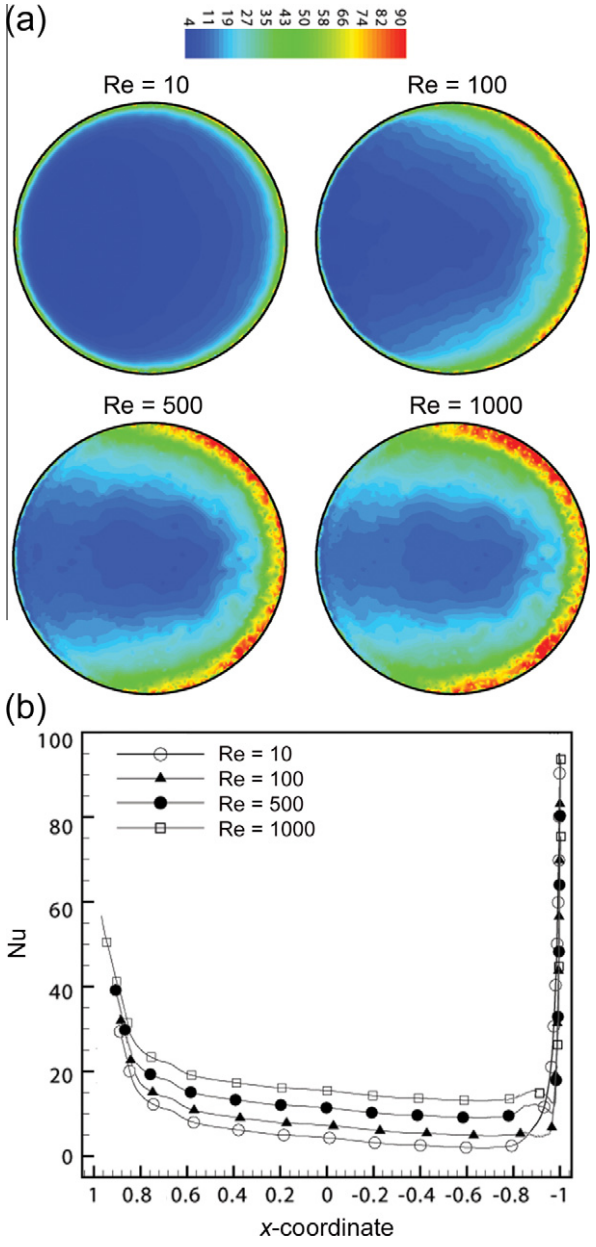

Fig. 28. Effect of Reynolds number: (a) Local Nusselt number distribution at the base of the drop of contact angle 105° and Pr = 6. (b) Variation of local Nusselt number as function of the *x*-coordinate that is aligned with the direction of surface motion.

Fig. 31 shows the variation of the average Nusselt number at the base of the droplet, as a function of Reynolds number and Prandtl number, for each of the drop shapes considered. As a rule, Nusselt numbers for a given droplet shape are higher for higher Prandtl number fluids. Comparing the three symmetric drops, the Nusselt number trend shows an inversion, i.e., at low Reynolds number viscous dominated regimes ($\sim$Re < 50), thermal diffusion through the droplet plays an important role and so the hydrophobic droplets show lower average Nusselt number. This trend gets reversed as convection starts dominating the thermal diffusion. Thus, at higher Reynolds numbers, the heat transfer coefficients of hydrophobic droplets are indeed superior. The effect of drop shape is to block flow driven by the motion of the solid wall, being the least for a drop of highest contact angle. The ease of fluid motion keeps the hydrodynamic boundary layer thin and contributes to higher heat transfer rates. The second factor contributing to the dependence of Nusselt number on contact angle is the drop height. It is a minimum for the deformed drop and increases with contact angle. Smaller drop heights prevent the formation of thermal boundary layers and consequently, lower Nusselt numbers. The deformed drop (whose contact angles vary from 55 to 105° with an average of 80°; Fig. 31(d)) shows data comparable to a symmetric drop with contact angle of 90°. The effect of Prandtl number on heat transfer rates is through a reduction in the thermal boundary-layer thickness, a result similar to heat transfer in channel flows.

Fig. 32 shows that the Nusselt number data closely scales with respect to Peclet number (=Re $\times$ Pr) for low Prandtl number liquids. Nusselt slightly increases with Peclet number. As in wall shear stress, Nusselt number decreases with increasing contact angle.

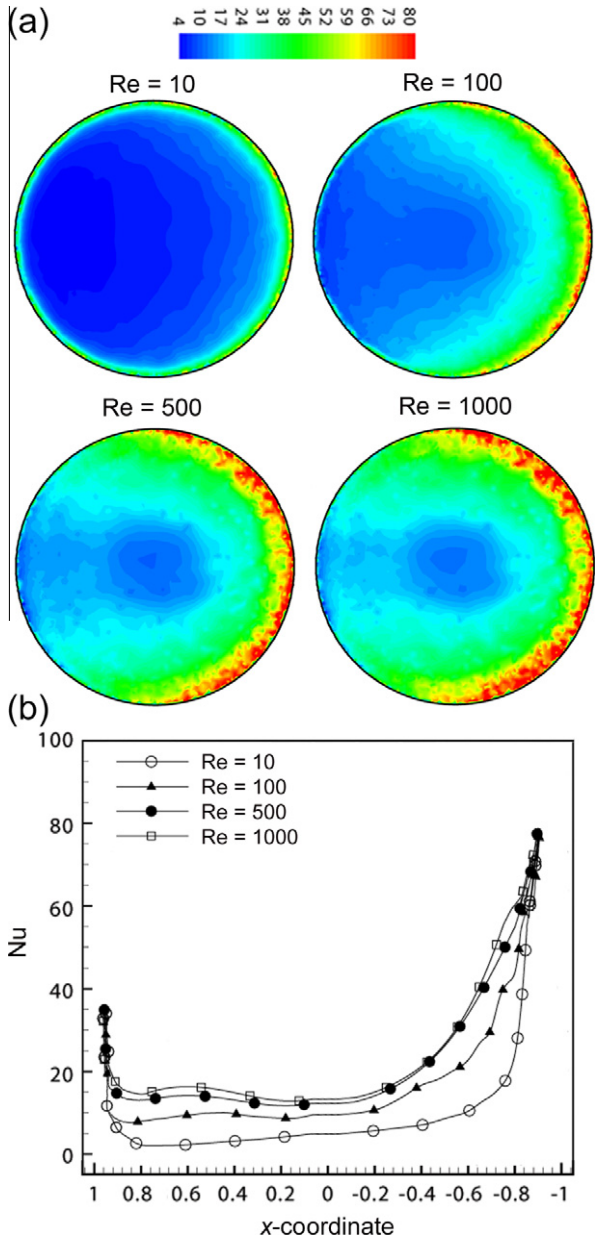

Fig. 29. Effect of Reynolds number: (a) Local Nusselt number distribution at the base of the drop of contact angle 120° and Pr = 6. (b) Variation of local Nusselt number as function of the *x*-coordinate that is aligned with the direction of surface motion.

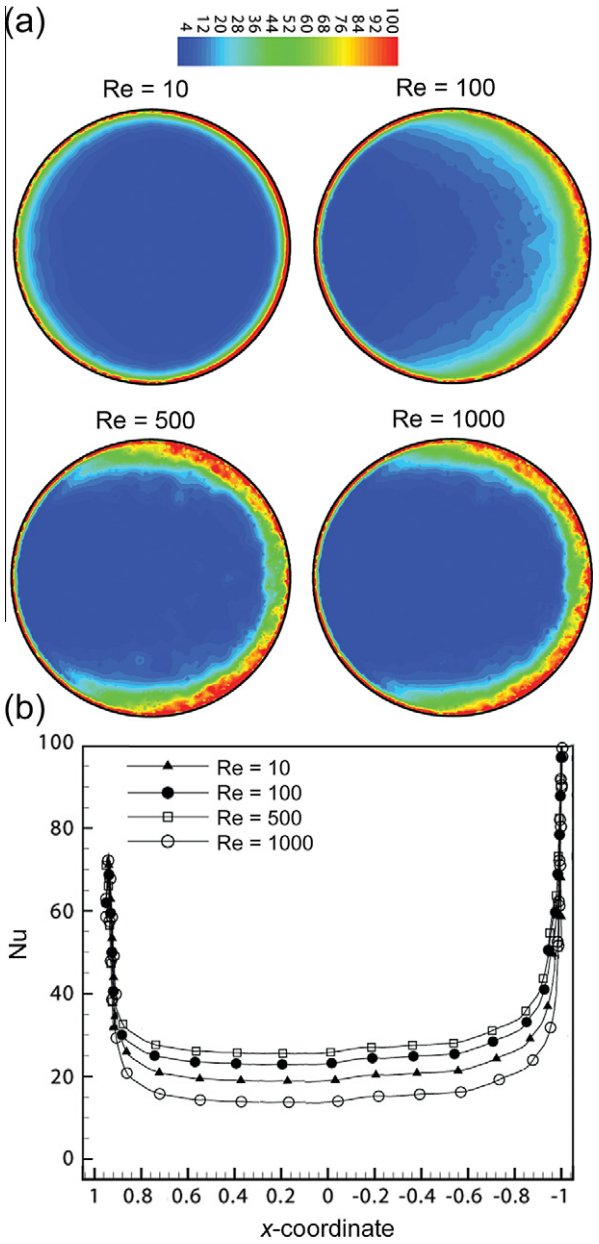

Fig. 30. Effect of Reynolds number: (a) Local Nusselt number distribution at the base of a deformed drop with contact angles 55° and 105° and Pr = 6. (b) Variation of local Nusselt number as function of the *x*-coordinate that is aligned with the direction of surface motion.

The best correlation through the Nusselt number data has been obtained as follows:

$$\begin{aligned} &\mathrm{Pr} \leqslant 0.3 \\ &\theta = 90^{\circ} \Rightarrow \overline{\mathrm{Nu}} = 10.5(\mathrm{Pe})^{0.0052} \\ &\theta = 105^{\circ} \Rightarrow \overline{\mathrm{Nu}} = 8.2(\mathrm{Pe})^{0.0058} \\ &\theta = 120^{\circ} \Rightarrow \overline{\mathrm{Nu}} = 7.4(\mathrm{Pe})^{0.00587} \\ &\theta = 80^{\circ}\,(\text{deformed}) \Rightarrow \overline{\mathrm{Nu}} = 12.2(\mathrm{Pe})^{0.0050} \end{aligned} \tag{30}$$

In view of a small exponent, Peclet number dependence can be dropped to a first approximation. The correlation for low Prandtl numbers liquids that includes contact angle (in radians) as a parameter is given by the best-fit equation:

$$\overline{\mathrm{Nu}} = 18.47\theta^{-1.26} \tag{31}$$

For liquids with higher Prandtl number:

$$\begin{aligned} &1 < \mathrm{Pr} < 30 \\ &\theta = 90^{\circ} \Rightarrow \overline{\mathrm{Nu}} = 7.3(\mathrm{Re})^{0.15}(\mathrm{Pr})^{0.1} \\ &\theta = 105^{\circ} \Rightarrow \overline{\mathrm{Nu}} = 6.72(\mathrm{Re})^{0.18}(\mathrm{Pr})^{0.1} \\ &\theta = 120^{\circ} \Rightarrow \overline{\mathrm{Nu}} = 5.12(\mathrm{Re})^{0.22}(\mathrm{Pr})^{0.1} \\ &\theta = 80^{\circ}\,(\text{deformed}) \Rightarrow \overline{\mathrm{Nu}} = 11.35(\mathrm{Re})^{0.12}(\mathrm{Pr})^{0.1} \end{aligned} \tag{32}$$

The correlation that includes contact angle as a parameter is given as:

$$\overline{\mathrm{Nu}} = 9.48\mathrm{Re}^{0.196}\mathrm{Pr}^{0.1}\theta^{-0.77} \tag{33}$$

The regression coefficient of curve fitting for Eqs. (30)–(33) was found to be better than 99.2%.

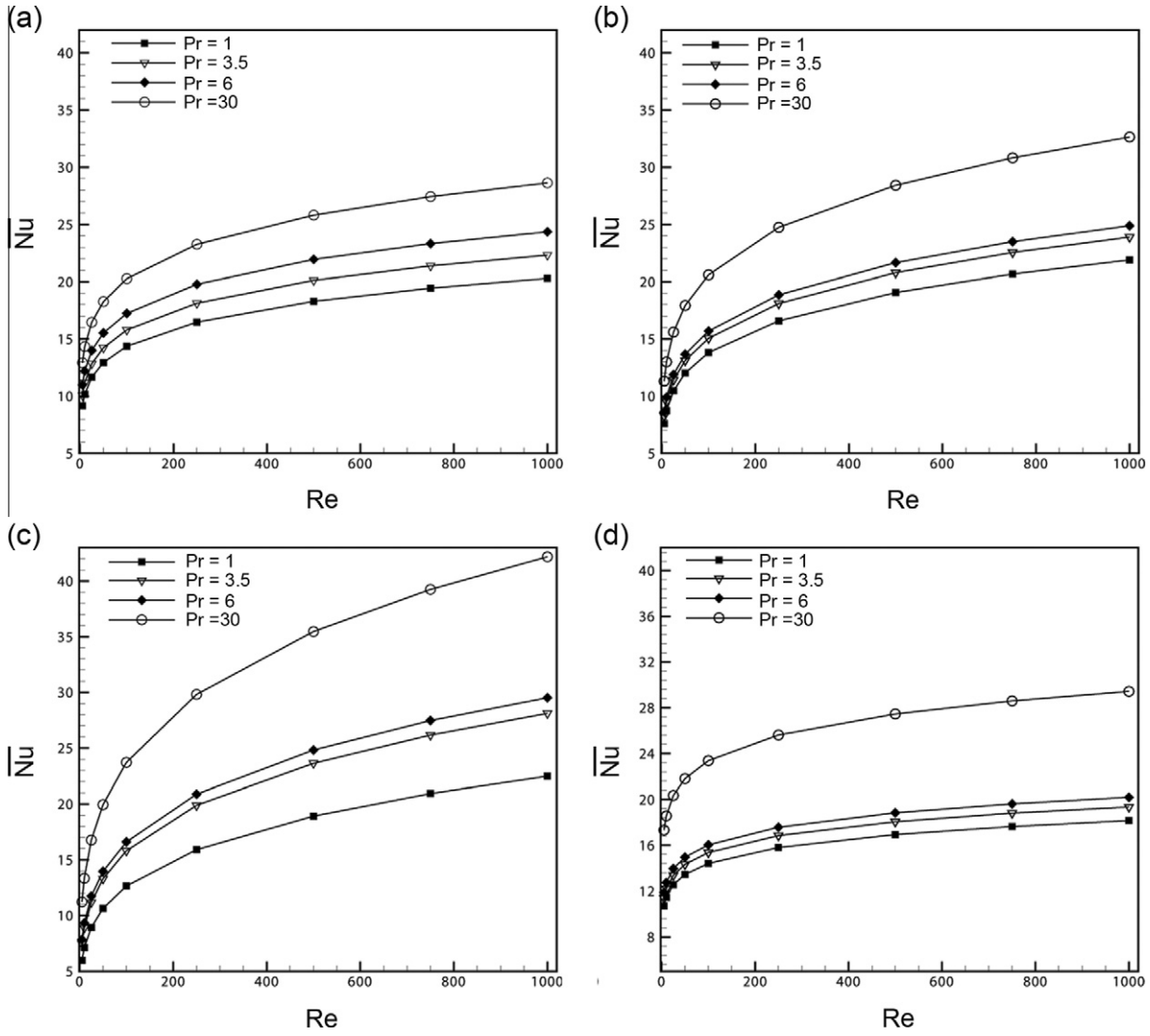

Fig. 31. Average Nusselt number as a function Reynolds number for various Prandtl numbers (>1) and shapes of the drop; contact angles (a) 90° (b) 105° and (c) 120° (d) deformed drop with advancing and receding angles of 105 and 55°.

The heat transfer rate can be combined with wall shear stress to form a figure of merit function. Such a function would represent the heat transfer enhancement obtainable from a liquid drop relative to the viscous shear penalty. The latter is to be seen as a price to be paid since large shear will result in early leaching of the substrate or its promoter coating. Large shear will also stabilize the drop and delay fall-off. The stabilization of the drop will inevitably result in lowering the heat transfer coefficient.

Using the correlations derived above, the figure of merit E is obtained for Pr > 1.0 as:

$$E = \frac{\overline{\mathrm{Nu}}}{\mathrm{Re} \times \overline{C}_f} = 0.1634(\mathrm{Re})^{0.166}(\theta)^{0.81}\mathrm{Pr}^{0.1} \tag{34}$$

For low Prandtl numbers (Pr < 0.3), the correlation for figure of merit is obtained as:

$$E = \frac{\overline{\mathrm{Nu}}}{\mathrm{Re} \times \overline{C}_f} = 0.318(\mathrm{Re})^{-0.03}(\theta)^{0.32} \tag{35}$$

From Eqs. (34) and (35), the figure of merit is seen to be a weak function of Reynolds number. This result arises from the fact that Nusselt number increases slightly with Reynolds number while the skin friction coefficient scales inversely with Reynolds number. Jointly, the weak dependence on Reynolds number is maintained. On the other hand, the figure of merit increases with contact angle, particularly for high Prandtl number fluids. This result indicates an advantage to be gained by making surfaces hydrophobic with respect to the concerned liquid.

5.2.3. Transport rates over inactive zones

A closer examination of the distribution of skin friction coefficient and local Nusselt number over the base of the drop (Figs. 16–19 and 27–29) shows that the central region experiences low shear and heat transfer that are relatively uniform. Large magnitudes of C_f and Nu are obtained closer to the edge of the drop. The central core at the base of the drop can be viewed as an inactive zone from the viewpoint of transport phenomena. These provide the lower limit of shear stress and heat transfer between the liquid and the solid surface.

Correlations based on the minimum values of skin friction coefficient and Nusselt numbers have been developed and are presented below. For skin friction coefficient, one obtains:

$$\begin{aligned}
&\theta = 90^{\circ} \Rightarrow \overline{C}_f = 4.57\mathrm{Re}^{-0.97} \\
&\theta = 105^{\circ} \Rightarrow \overline{C}_f = 3.64\mathrm{Re}^{-0.97} \\
&\theta = 120^{\circ} \Rightarrow \overline{C}_f = 2.78\mathrm{Re}^{-0.97} \\
&\theta = 80^{\circ}(\text{deformed}) \Rightarrow \overline{C}_f = 5.43\mathrm{Re}^{-0.97}
\end{aligned} \tag{36}$$

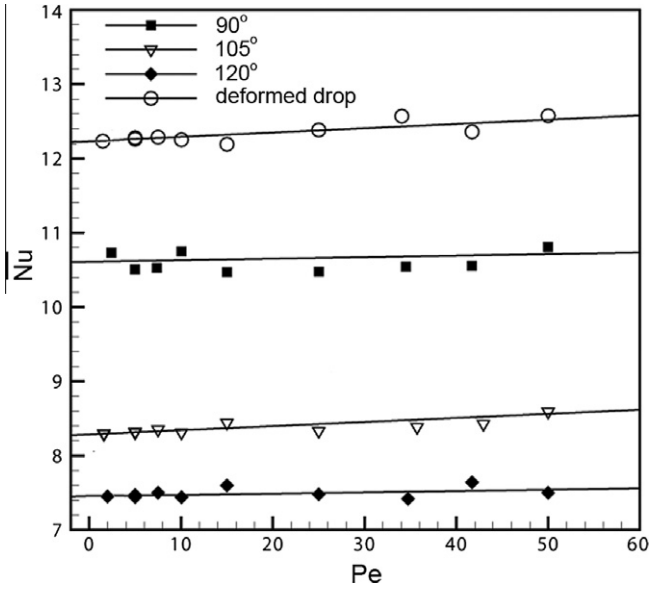

Fig. 32. Average Nusselt number as a function of Peclet number for drops of various shapes for liquid metal ($Pr \leqslant 0.3$).

Including contact angle as a parameter, skin friction coefficient is obtained as

$$\overline{C}_f = 9.49\mathrm{Re}^{-0.97}\theta^{-1.58} \tag{37}$$

Comparing Eqs. (36) and (37) with Eqs. (28) and (29), a reduction in C_f by a factor of around 6 is to be seen. There is no change in the exponents of the Re and angle θ.

For Nusselt number, the correlation based on the minimum value of heat flux at the base of the drop is obtained as:

$$\begin{aligned} &1 < \mathrm{Pr} < 30 \\ &\theta = 90^{\circ} \Rightarrow \overline{\mathrm{Nu}} = 4.4(\mathrm{Re})^{0.15}(\mathrm{Pr})^{0.1} \\ &\theta = 105^{\circ} \Rightarrow \overline{\mathrm{Nu}} = 4.1(\mathrm{Re})^{0.18}(\mathrm{Pr})^{0.1} \\ &\theta = 120^{\circ} \Rightarrow \overline{\mathrm{Nu}} = 3.08(\mathrm{Re})^{0.22}(\mathrm{Pr})^{0.1} \\ &\theta = 80^{\circ}(\text{deformed}) \Rightarrow \overline{\mathrm{Nu}} = 6.5(\mathrm{Re})^{0.12}(\mathrm{Pr})^{0.1} \end{aligned} \tag{38}$$

The average correlation including all contact angles is obtained as

$$\overline{\mathrm{Nu}} = 8.12\mathrm{Re}^{0.20}\mathrm{Pr}^{0.1}\theta^{-0.8}(\mathrm{Pr} > 1) \tag{39}$$

For low Prandtl numbers, the respective correlations are:

$$\begin{aligned} &\mathrm{Pr} \leqslant 0.3 \\ &\theta = 90^{\circ} \Rightarrow \overline{\mathrm{Nu}} = 7.99(\mathrm{Pe})^{0.0052} \\ &\theta = 105^{\circ} \Rightarrow \overline{\mathrm{Nu}} = 6.58(\mathrm{Pe})^{0.0058} \\ &\theta = 120^{\circ} \Rightarrow \overline{\mathrm{Nu}} = 5.56(\mathrm{Pe})^{0.00587} \\ &\theta = 80^{\circ}(\text{deformed}) \Rightarrow \overline{\mathrm{Nu}} = 9.27(\mathrm{Pe})^{0.0050} \end{aligned} \tag{40}$$

The average Nusselt number correlation that includes all angles is

$$\overline{\mathrm{Nu}} = 14.12\theta^{-1.26} \tag{41}$$

The reduction in the Nusselt number is by a factor of 1.3-1.8 when compared to the average based on the entire drop base area. These results reveal that the contact line plays an important role in fixing shear stress and heat transfer. Consequently, the contact angle is an important parameter in transport phenomena through single drops.

6. Conclusions

Three-dimensional simulation of flow and heat transfer in pendant drops of various shapes moving on a solid surface has been reported. The drop shape is characterized by the apparent contact angle when symmetric, and advancing and receding angles for a deformed geometry. Droplet flow Reynolds numbers up to 1000 have been considered while the Prandtl number ranges from 0.005 to 30. Results show that a circulation pattern is setup within the drop. The center of the circulation pattern where velocity is zero moves towards the solid surface at higher Reynolds numbers. Pressure and wall shear stress are nearly uniform at the base of the drop, except at the periphery where large changes take place. The average skin friction coefficient scales as $\sim\mathrm{Re}^{-1}$ with Reynolds number and increases for smaller contact angles. Heat transfer in drops of high Prandtl numbers is characterized by the appearance of thermal boundary layers. Temperature distribution across the drop shows large gradients near the walls while temperature inversion is seen in the core. Inversion can be explained by the three-dimensionality of the flow field particularly at high Reynolds numbers. At lower Prandtl numbers, diffusive transport governs heat transfer rates and a near-linear variation of temperature is obtained. Wall heat transfer rates are uniform over the base of the drop and take on extreme values around the periphery. For a wall moving towards the left, heat fluxes at the right periphery are greater than at the left. Nusselt number increases as the contact angle decreases. The core of the base of the drop is a region of low shear stress and heat flux. For $\mathrm{Pr} > 1$, the average Nusselt number scales as Re^m where exponent m is in the range 0.12–0.22 and with Prandtl number as $\mathrm{Pr}^{0.1}$. For low Prandtl numbers, Nusselt number is practically independent of Peclet number but increases when the contact angle is diminished. The figure of merit improves with the contact angle, and hence the hydrophobicity of the surface. The results of the present study can be applied to a drop ensemble, as in a continuous quasi-steady dropwise condensation process.

Acknowledgment

Financial support provided by the Board of Research in Nuclear Sciences, Department of Atomic Energy, Government of India is gratefully acknowledged.

References

[1] J. Berthier, Microdrops and Digital Microfluidics, in: William Andrew, second ed., Hemisphere Publishing Corporation, NY, USA, 2008, pp. 75–179.
[2] V. Pratap, N. Moumen, R. Subramanian, Thermocapillary motion of a liquid drop on a horizontal solid surface, Langmuir 24 (2008) 2185–5193.
[3] C.G. Furmidge, The sliding drop on solid surfaces and a theory for a spray retention, J. Colloid Sci. 17 (1962) 309–324.
[4] R.N. Leach, F. Stevens, S.C. Langford, J.T. Dickinson, Dropwise condensation: experiments and simulations of nucleation and growth of water drops in a cooling system, Langmuir 22 (2006) 8864–8872.
[5] J.W. Rose, Dropwise condensation theory and experiments: a review, Proc. Inst. Mech. Eng. 216 (2002) 115–118.
[6] B.S. Sikarwar, N.K. Battoo, S. Khandekar, K. Muralidhar, Dropwise condensation underneath chemically textured surfaces: simulation and experiments, ASME J. Heat Transfer 133 (2) (2011) 021501–021515.
[7] B.J. Briscoe, K.P. Galvin, The sliding of sessile and pendent droplets, the critical condition, J. Colloid Interface Sci. 52 (1991) 219–229.
[8] L.Y. Lee, T.H. Fang, Y.M. Yang, J.R. Maa, The enhancement of dropwise condensation by wettability modification of solid surface, Int. Commun. Heat Mass Transfer 25 (8) (1998) 1095–1103.
[9] R.S. Subramanian, N. Moumen, J.B. McLaughlin, Motion of a drop on a solid surface due to a wettability Gradient, Langmuir 21 (2005) 11844–11849.
[10] A. Leipertz, A.P. Fröba, Improvement of condensation heat transfer by surface modification, in: S.C. Mishra, (Ed.), Proceedings of the Seventh ISHMT-ASME International Heat and Mass Transfer Conference, IIT Guwahati, India, K7 2006, pp. k85–k99.
[11] G.D. Bansal, S. Khandekar, K. Muralidhar, Measurement of heat transfer during dropwise condensation of water on polyethylene, Nanoscale Microscale Thermophys. Eng. 13 (2009) 184–201.
[12] C.W. Extrand, Y. Kumara, Liquid drop on an inclined plane: the relation between apparent contact angles, drop shape and retentive force, J. Colloid Interface Sci. 170 (1995) 515–521.

[13] E.B. Dussan, On the ability of drops or bubbles to stick to non-horizontal surface of solids, J. Fluid Mech. 151 (1985) 1–20.
[14] X. Li, C. Pozrikidis, Shear flow over a liquid drop adhering to a solid surface, J. Fluid Mech. 307 (1996) 167–190.
[15] P. Dimitrakopoulos, Deformation of droplet adhering to a solid surface in shear flow: onset of interfacial sliding, J. Fluid Mech. 580 (2006) 451–466.
[16] A.I. Elsherbine, A.M. Jacobi, Liquid drops on vertical and inclined surfaces II. An experimental study of drop geometry, J. Colloid Interface Sci. 273 (2004) 566–575.
[17] A.I. Elsherbine, A.M. Jacobi, Retention forces and apparent contact angles for critical liquid drops on non-horizontal surfaces, J. Colloid Interface Sci. 299 (2006) 841–849.
[18] Ho.-Young. Kim, H. Lee, B.H. Kang, Sliding of drops down an inclined solid surface, J. Colloid Sci. 247 (2002) 372–382.
[19] H. Huang, D. Liang, B. Wetton, Computation of a moving drop/bubble on a solid surface using a front-tracking method, Commun. Math. Sci. 2 (suppl. 2) (2004) 535–552.
[20] L. Gao, T.J. McCarthy, Apparent contact angle hysteresis explained, Langmuir 22 (2006) 6234–6237.
[21] S. Suzuki, A. Nakajima, M. Sakai, J. Song, N. Yoshida, Y. Kameshima, K. Okada, Sliding acceleration of water droplets on a surface coated with fluoroalkysline and octadecyltrimethoxysilane, Surf. Sci. 600 (2006) 2214–2219.
[22] M. Sakai, J. Song, N. Yoshida, S. Suzuki, Y. Kameshima, A. Nakajima, Direct observation on internal fluidity in a water droplet during sliding on hydrophobic surfaces, Langmuir 22 (2006) 4906–4909.
[23] N.L. Grand, A. Daerr, L. Limit, Shape and motion of drops sliding down an inclined plane, J. Fluid Mech. 541 (2005) 293–315.
[24] N. Yoshida, Y. Abe, H. Shigeta, A. Nakajima, K. Ohsaki, T. Watanable, Sliding behavior of droplet on flat polymer surface, J. Am. Chem. Soc. 128 (2006) 743–747.
[25] S. Daniel, M.K. Chaudhury, J.C. Chen, Fast drop movements resulting from the phase-change on a gradient surface, Science 29 (2001) 633–636.
[26] M. Sakai, A. Hashimoto, Image analysis system for evaluating sliding behavior of a liquid droplet on a hydrophobic surface, Rev. Sci. Instrum. 78 (2007) 045103–045109.
[27] S. Suzuki, A. Nakajima, M. Sakai, J. Song, N. Yoshida, Y. Kameshima, K. Okada, Slipping and rolling ratio of sliding acceleration for a water droplet sliding on fluoroalkylsilane coating of different roughness, Chem. Lett. 37 (2008) 58–59.
[28] A.K. Das, P.K. Das, Simulation of drop movement over an inclined surface using smoothed particle hydrodynamics, Langmuir 25 (2009) 11459–11466.
[29] A.W. Date, Solution of transport equations on unstructured meshes with cell centered collocated variables Part I: Discretization, Int. J. Heat Mass Transfer 48 (2005) 1117–1127.
[30] B.S. Sikarwar, S. Khandekar, S. Agrawal, S. Kumar, K. Muralidhar, Dropwise condensation studies on multiscales, J. Heat Transfer Eng. 33 (3/4) (2012). Special Issue: Advances in Heat Transfer.
[31] B.S. Sikarwar, K. Muralidhar, S. Khandekar, Flow and heat transfer in a liquid drop sliding on an inclined plane, in: K.S. Iyer (Ed.), Proceedings of the Ninth ISHMT-ASME International Heat and Mass Transfer Conference, IIT Mumbai, India, 2010, pp. 1322–1329.
[32] N.T. Frink, P. Paresh, P. Shahyar, A fast upwind solver for the Euler equations on three dimensional unstructured meshes, AIAA 91 (1991) 0102–0108.
[33] P.N. Shankar, M.D. Deshpande, Fluid mechanics in the driven cavity, Annu. Rev. Fluid Mech. 32 (2000) 93–136.
[34] E. Kreyszig, Advanced Engineering Mathematics, ninth ed., John Wiley and Sons, Inc., New York, 2006. pp. 535–587.
[35] T. Saitoh, K. Hirose, High-accuracy bench mark solutions to natural convection in a square cavity, Comput. Mech. 4 (1989) 417–427.